Geomorphology 488 (2025) 109955

Contents lists available at ScienceDirect

Geomorphology

journal homepage: www.journals.elsevier.com/geomorphology

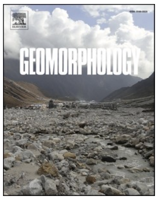

Diapiric and tectonic geomorphology of the river-damming Jahani salt extrusion associated with the strike-slip Kareh Bas Fault, including DInSAR displacement data (Zagros Mountains, Iran)

Francisco Gutiérrez [a,*], Mahmud Haghshenas Haghighi [b], Issa Ilyati [c], Mahdi Motagh [d], Miren del Val [e]

[a] Department of Earth Sciences, University of Zaragoza, Spain
[b] Institute of Photogrammetry and GeoInformation, Leibniz University Hannover, Germany
[c] Department of Earth Sciences, Shiraz University, Iran
[d] German Research Center for Geoscience at Postdam, Germany
[e] Centro Nacional de Investigación sobre la Evolución Humana (CENIEH), Burgos, Spain

ARTICLE INFO

Keywords:
Salt diapir
Paleoearthquake
Salt-glacier dam
Paleolake
Salt sheet

ABSTRACT

The Fars Arc of the Zagros Fold-and-Thrust Belt hosts the most remarkable examples of salt extrusions worldwide, within a context of rapid collision-related deformation and high seismic activity. Hormuz salt extrusions in the western Fars Arc form rows associated with >200 km long dextral strike-slip faults, which constitute major seismic sources. This work is focused on the Jahani salt fountain and the associated Kareh Bas Fault. The Kareh Bas Fault is interpreted as a supra-salt tear fault controlled by thickness variations in the Hormuz salt detachment and associated rows of precursor diapirs. The precursor Jahani diapir likely induced the segmentation of the S-propagating Kareh Bas Fault, generating a releasing stepover that facilitated salt emergence. OSL dating of +40 m terrace deposits of the Shur River deformed by the Kareh Bas Fault reveals that the fault sourced two paleoearthquakes before and around 14.7–13.8 ka, and indicates a long-term fluvial incision rates of 2.7–2.9 mm/yr. The emerged Jahani diapir (68 km^2, 918 m in local relief) is a salt fountain comprising a protruding summit dome and laterally spreading salt glaciers (i.e., namakiers). The northern namakier has been trimmed by the Shur River, generating an exceptional salt escarpment 6 km long and >400 m high. Masses of disconnected Hormuz rocks on the opposite margin of the valley and paleolake deposits found upstream and dated by OSL at 28 ± 5 ka, indicate that the Shur River has experienced multiple damming episodes, likely during dry periods. This work documents for the first time the damming of a major drainage by a salt glacier and the creation of a lake. DInSAR data reveal an overall progressive displacement pattern in the Jahani salt fountain characterised by a rising summit dome (1–2 cm/yr) and laterally spreading namakiers with distally decreasing horizontal displacement rates (1–2 cm/yr) and some uplift in the frontal sectors. This general pattern is altered in the northern sector, where the debuttressed salt extrusion rapidly flows towards the deeply entrenched Shur valley at horizontal and vertical rates of around 10–15 cm/yr. The presented displacement data invalidate a previous work, that based on inadequate theodolite displacement measurements of the order of m/yr, suggested that the is one of the most vigorously rising salt extrusions on Earth.

1. Introduction

The Zagros orogen is one of the most seismically active and rapidly deforming mountain belts in the world, though it has relatively scarce documented paleoseismic evidence. The lack of evidence can be attributed to two main reasons: (1) a significant proportion of the large earthquakes are sourced from blind faults, which upward propagation is impeded by evaporitic detachments such as the Neoproterozoic-Cambrian Hormuz salt (lower mobile group) and the Miocene Gachsaran Formation (upper mobile group) (Berberian, 1995; Talebian and

---

* Corresponding author.
E-mail addresses: fgutier@unizar.es (F. Gutiérrez), mahmud@ipi.uni-hannover.de (M.H. Haghighi), motagh@gfz-potsdam.de (M. Motagh), miren.delval@cenieh.es (M. del Val).

https://doi.org/10.1016/j.geomorph.2025.109955
Received 17 April 2025; Received in revised form 16 June 2025; Accepted 2 August 2025

Jackson, 2004; Molinaro et al., 2005); and (2) Quaternary sediments and landforms have received limited attention as markers of recent deformation and archives of past seismic activity (e.g., Gutiérrez et al., 2023a). The fold festoon of the Fars Arc hosts more than one hundred extrusions of Hormuz salt that display a morpho-chronological variety, including growing domes, salt fountains with a summit dome and spreading salt glaciers or namakiers (i.e., salt glacier in Persian), wasting salt droplets, and degraded domes (Jahani et al., 2007; Talbot and Pohjola, 2009; De Waele and Gutiérrez, 2022). These are widely considered as precursor diapirs rejuvenated during the SW-propagating Zagros orogeny, and that have functioned as fold and fault localizers and enhancers (Jahani et al., 2009, 2017; Gutiérrez et al., 2024). In the western Fars Arc, the salt extrusions are associated with orogen-oblique strike slip faults (Talbot and Alavi, 1996), forming the most remarkable example strike-slip fault and salt systems worldwide (Jackson and Hudec, 2017). These are highly dynamic and poorly investigated environments, including (1) >200 km long strike-slip faults with GPS-derived slip rates of around 3.5 mm/yr (Vernant et al., 2004), that pose a major threat to large populations, such Shiraz city with over 1.6 million residents, which was largely destroyed by an earthquake in 1853; (2) mobile salt extrusions with poorly constrained displacement rates; (3) salt glaciers that interact with major drainages.

This work is focused on the Jahani diapir and the associated dextral Kareh bas Fault. The Jahani diapir has emerged at the surface, forming a salt extrusion that has reached the salt fountain evolutionary stage, showing a protruding summit dome and salt glaciers that flow laterally over the surrounding lowlands. The Jahani salt extrusion, with ca. 1 km of local relief and located in a semiarid environment (precipitation ca. 350 mm/yr), is considered to be one of the most vigorously rising emergent diapirs in the Zagros, with putative displacement rates of the order of meters per year (Talbot et al., 2000). A remarkable feature of this salt fountain is that the Shur River has trimmed the northern salt glacier generating a 6 km long salt escarpment that reaches 425 m in local relief (Gutiérrez et al., 2025). A number of works have been previously published dealing with the geomorphology, hydrology and dynamics of the Jahani salt extrusion. Talbot et al. (2000) presented poorly consistent theodolite measurements of ground displacement at Jahani, sal and claimed that it is one of the most rapidly rising salt extrusions on Earth. Based on the inferred average uplift rates at the summit dome and a mass balance calculation accounting for salt dissolution, they estimated that the onset of salt emergence occurred at around 55 ka. Bruthans et al. (2008) measured erosion on rock salt exposures (rillenkarren and gullies) in Jahani using plastic pegs 11 cm long. In 2000 they installed 14 pegs that were measured in 2004, but only 4 of them persisted, while the remaining 10 were released providing minimum erosion values. In 2004 four additional pegs were installed and subsequently measured in 2005. Based on these data, they proposed a mean annual vertical denudation rate of 80–120 mm/yr for salt exposures in the Jahani salt extrusion. Bruthans et al. (2009) characterised the mineralogical composition of rock salt (one sample; 93.1 % halite, 4.7 % silicates and oxides, <2.1 % gypsum and anhydrite) and residual capsoils at Jahani (average of nine samples; 38.9 % silicates and oxides, 30.5 % carbonates, 27.8 % gypsum/anhydrite, 2.8 % halite). Abirifard et al. (2017) described the polygonal karst landscape developed in the summit dome and salt glaciers of Jahani, and characterised the local autogenic karst hydrology, including numerous permanent brine springs saturated with respect to halite. These authors, using discharge and hydrochemical data estimated that the total annual mass of dissolved halite in the Shur River increases from 2530 to 319,725 t in the section where it interacts with the Jahani salt extrusion. Bruthans et al. (2017) documented a flash flood event at Jahani (30 March 2009; 64 mm rainfall), which resulted in significant runoff, flooding of karst depressions, and a flashy discharge rise in some brine springs accompanied by water dilution (undersaturated with respect to halite). Bruthans et al. (2024) documented 18 caves (shafts and vadose canyons) in the namakiers of Jahani with a total length of 3.5 km. According to radiocarbon ages from detrital deposits, the longest caves (White Foam, 1262 m long; Hidden Creek, 478 m; Waterfall 424 m) formed over ca. 600 years, recording rapid development and incision rates. Gutiérrez et al. (2025) characterised the surface karst geomorphology of the Jahani salt extrusion and provided a review on the previous studies conducted in this remarkable emergent diapir.

The primary objectives of this work include: (1) to better understand the mechanical relationship between the Kareh Bas Fault and the Jahani salt diapir; (2) to constrain the timing of paleoearthquakes on the Kareh Bas fault by Optically Stimulated Luminescence dating; (3) to document and date for the first time the damming of a major drainage by a salt glacier and the creation of an upstream lake; (4) to provide more accurate estimates of spatial-temporal patterns of surface displacement over the Jahani salt diapir using interferometric synthetic aperture radar (InSAR) time-series. The obtained information provides the basis for discussing previous geodetic measurements and age estimates on the timing of salt emergence.

2. Geological setting

2.1. Geotectonic setting and general geological history

The Zagros Fold-and-Thrust Belt, with a general NW-SE structural grain, is related to the collision between the Arabian and Eurasian plates, currently converging with an orogen-oblique NNE vector at 20–25 mm/yr (Vernant et al., 2004; Walpersdorf et al., 2006) (Fig. 1A). The Zagros Belt is divided into two main zones separated by the High Zagros Fault: (1) the High Zagros to the NE, and (2) the Simply Folded Belt to the SW. The Simply Folded Belt comprises three domains with different detachment horizons and structural features bounded by major strike-slip faults, from NW to SE (Motiei, 1993; Sepehr and Cosgrove, 2004) (Fig. 1B): (1) the Lurestan Arc west of the Balarud Fault; (2) the Dezful Embayment; and (3) the Fars Arc, east of the Kazerun-Borazjan fault system, where the Jahani salt extrusion is located. Here, the main detachment corresponds to the 1–1.5 km thick Hormuz salt of late Neoproterozoic-early Cambrian age, which has formed many salt diapirs and extrusions (Talbot and Alavi, 1996).

The Hormuz salt was accumulated in grabens controlled by N-trending faults (Kent, 1979; Talbot and Alavi, 1996; Jahani et al., 2017). Throughout most of the Phanerozoic the region was dominated by sedimentation, mainly in shallow marine environments (Neo-Tethys ocean) (Stöklin, 1968). The continent-continent collision led to the built up of the Zagros Mountain Belt in the Late Cenozoic, accompanied by progressive SW propagation of the deformation towards the foreland (Talbot and Alavi, 1996). Syntectonic deformation (growth strata and angular unconformities) indicates that shortening started at the Eocene-Oligocene transition in the NE of the Simply Folded Belt and advanced to the SW during deposition of progressively younger formations (Hessami et al., 2001a; Gutiérrez et al., 2024). The initiation of significant morphogenetic folding and relief creation under continental conditions is recorded by the time-transgressive basal unconformity of the syn-orogenic clastics (molasses) of the Bakhtyari Formation (Hessami et al., 2001a; Mouthereau et al., 2007; Gutiérrez et al., 2023a, 2023b), gradually younger to the SW (Homke et al., 2004; Fakhari et al., 2008; Khadivi et al., 2010; Ruh et al., 2014; Vergés et al., 2019), revealing that the onset of a number of processes varies across the orogenic wedge, including: (1) deformation structures such as folds, reverse faults and strike-slip faults; and (2) rejuvenation of precursor diapirs by contractional loading and eventually their extrusion (Talbot and Alavi, 1996; Letouzey and Sherkati, 2004; Gutiérrez et al., 2024).

2.2. Diapirs and strike-slip faults in the Fars Arc

The Fars Arc is a festoon of folds detached along the Hormuz salt that decouples a 12–15 km thick overburden from the rigid basement (Jahani et al., 2007, 2009) (Fig. 1C). This structural domain displays more than

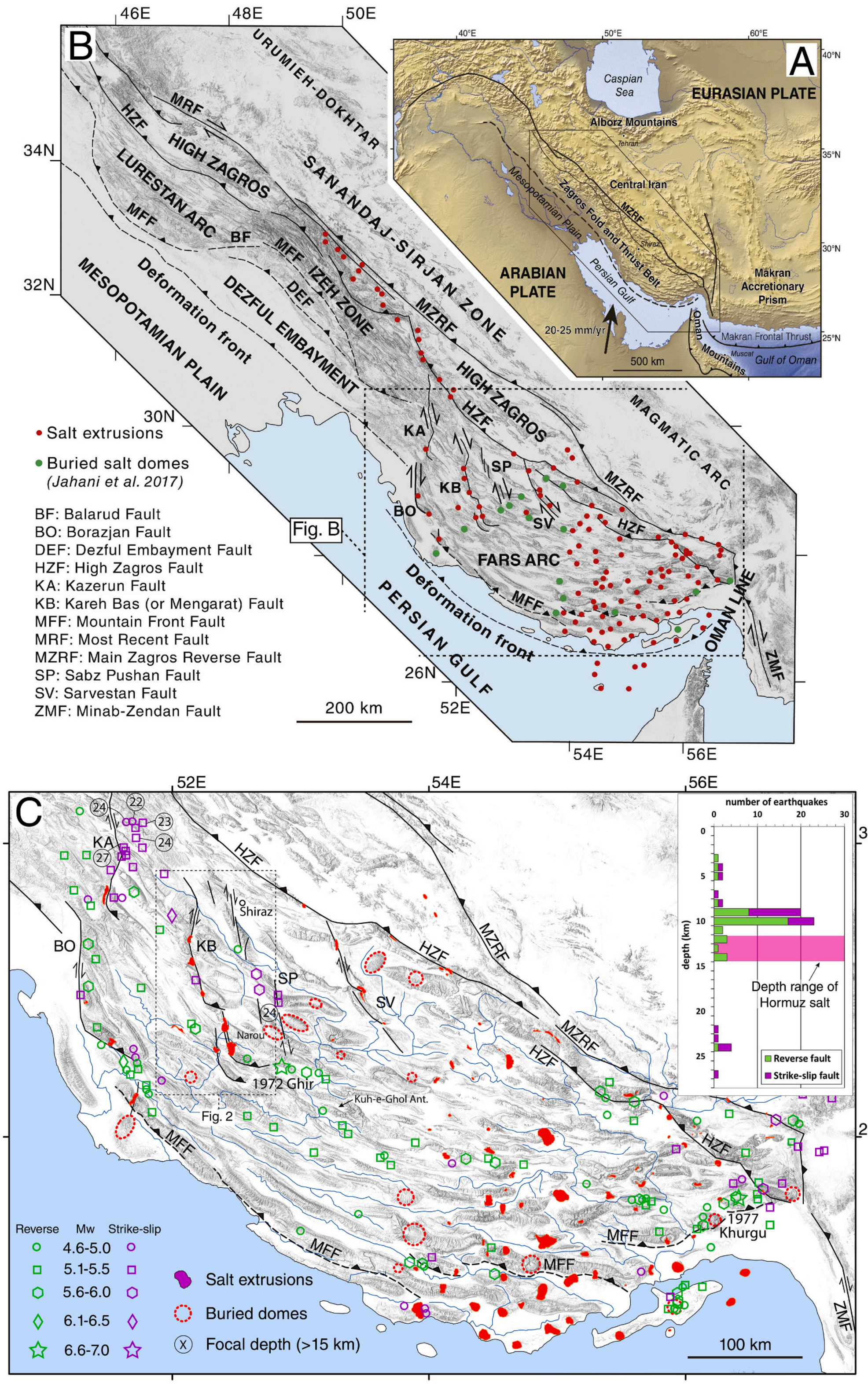

Fig. 1. A: Geotectonic setting of the Zagros Fold and Thrust Belt related to the ongoing oblique convergence between the Arabian and Eurasian plates. B: Sketch of the Zagros orogen (lower left) showing the distribution of the main structural zones, faults, and salt diapirs, both emerged (red circle) and buried (green circle). Vector displacement of the Arabian Plate from GPS data published by Vernant et al. (2004). C: Map of the Fars Arc of the Simply Folded Belt showing the diapirs of Hormuz salt (emergent and buried), the main faults (names indicated in fig. A), and the epicentres from the relocated earthquake catalog (1962–2018; error <5 km) of Karasözen et al. (2019), differentiated by the dominant focal mechanism and M_w (moment magnitude) intervals. Inset shows the distribution of focal depths in the western Fars Arc, between 51°E and 53.5°E, and the depth range of Hormuz salt (ca. 12–15 km) inferred by Jahani et al. (2009, 2017) on the basis of seismic profiles. The focal depths greater to 15 km are indicated in the map by encircled numbers (Adapted from Gutiérrez et al., 2024).

one hundred emergent or buried Hormuz salt diapirs (Kent, 1958, 1979; Jahani et al., 2009, 2017; Gutiérrez et al., 2023b). Salt diapirs in the Fars Arc tend to occur associated with anticlines and are distributed in two well differentiated sectors (Fig. 1C): (1) the eastern limb of the Fars Arc, where most diapirs lack spatial relationship with faults; and (2) the western sector of the Fars Arc, where the majority of the diapirs occur associated with N- to NNW-trending right-lateral strike-slip faults. Ample stratigraphic and structural evidence indicate that these are mostly pre-shortening salt walls and stocks (Harrison, 1930; Kent, 1979; Talbot and Jarvis, 1984; Talbot and Alavi, 1996; Sherkati et al., 2006; Jahani et al., 2007, 2009, 2017; Snidero et al., 2019) that experienced rejuvenation by contractional loading (i.e., squeezing) during the Cenozoic collisional deformation (Jahani et al., 2007, 2017; Gutiérrez et al., 2023b). The weak precursor salt plugs played an important role in the deformation of the foreland, acting as strain localizers and enhancers. Salt diapirs controlled the nucleation lateral propagation of anticlines (Callot et al., 2007; Jahani et al., 2007, 2009; Gutiérrez et al., 2023b, 2024). Additionally, belts of salt walls and stocks associated with N- and NNW-trending infra-salt normal faults that controlled thickness variations during Hormuz sedimentation, have guided the development of strike-slip supra-salt tear faults (e.g., Kazerun-Borazjan Fault, Kareh Bas Fault; Jahani et al., 2017; Hassanpour et al., 2018; Gutiérrez et al., 2024) (Figs. 1C, 2).

Tectonic structures in the western Fars Arc display strain partitioning within a context of NNE oblique convergence (Fig. 1B, C). The orogenic deformation is accommodated by NW-SE-oriented longitudinal folds and reverse faults, plus right-lateral displacement along four oblique N- to NNW-trending strike-slip fault systems (Berberian, 1995; Hessami et al., 2001b; Talbot and Alavi, 1996; Authemayou et al., 2006; Jahani et al., 2017; Hassanpour et al., 2018; Gutiérrez et al., 2024), including from W to E (Berberian and Tchalenko, 1976; Berberian, 1995): (1) the Kazerun-Borazjan fault system; (2) the Kareh Bas (or Mengarak) fault system; (3) the Sabz Pushan fault zone; and (4) the Sarvestan Fault (Fig. 1B, C). These faults, roughly parallel to the plate convergence vector, display the following features (Berberian, 1995; Hessami et al., 2001b; Authemayou et al., 2006, 2009; Faghih et al., 2016; Hassanpour et al., 2018; Gutiérrez et al., 2024; Nezamzadeh et al., 2024): (1) right-lateral offset of folds; (2) alignments of salt extrusions; (3) several geometric segments, often terminating at their southern end with sharp reverse-fault eastward bends associated with the steeper or overturned southern limb of anticlines; and (4) ascribable damaging earthquakes. Tavakoli et al. (2008), based on data from a dedicated GPS network, measured horizontal slip rates of 3.6 ± 0.6 mm/yr and 3.4 ± 0.3 mm/yr across the Kazerun Fault and the Kareh Bas Fault, respectively.

Regarding the Kareh Bas fault system, Gutiérrez et al. (2024) differentiated three geometric segments with an aggregate length of 220 km (Fig. 2). These are NNW-SSE right-lateral strike-slip faults that connect at their southern termination with longitudinal WNW-ESE-striking and S-verging reverse faults associated with the southern steeper to overturned limb of anticlines (i.e., contractional bend terminations). The 120 km long Kareh Bas N segment, 25 km west of Shiraz city, displays two pull-apart basins with conspicuous geomorphic expression: (1) the 11.5 km long Kareh Bas Basin associated with the Dalu Anticline, and (2) the 11 km long and 1.8 km wide Dandenjan Basin associated with the Dandenjan Anticline and the Dandenjan salt extrusion, analysed by Gutiérrez et al. (2024). The 56 km long Kareh Bas S segment shows a left-stepping en enchelon arrangement with respect to the N segment, both linked by the Dandenjan reverse fault at the step-over (Fig. 2). The Kareh Bas S segment terminates at the Surmeh reverse fault along the southern limb of the SSW verging Surmeh Anticline. The 44 km long Kareh Bas SW segment shows a right-stepping and overlapping distribution with respect to the S segment and terminates at an eastward contractional bend defined by the Kalagh reverse fault. The five salt extrusions located along the Kareh Bas N and S segments display a N-S morphological and morphometric gradation. This evidence suggests a successive emergence of salt diapirs associated with the southward propagation of the fault system and the creation of new structural discontinuities for salt breakout from precursor diapirs at contracting anticlines. (Gutiérrez et al., 2024) (Fig. 2).

Fig. 1C shows the distribution of historical earthquakes and epicentres from the relocated earthquake catalog (1962–2018; error < 5 km) of Karasözen et al. (2019), classified according to the dominant focal mechanism (95 reverse, 47 strike-slip) and the moment magnitude (M_W) intervals. The inset graph shows the distribution of focal depths in the western Fars (between 51°E and 53.5°E), and the depth range of the regional detachment (Hormuz salt; ca. 12–15 km) inferred by Jahani et al. (2009, 2017) on the basis of seismic profiles and geological cross-sections. These figures shows that: (1) around 70 % of the strike-slip earthquakes of the Fars Arc are associated with the strike-slip faults of the western Fars; (2) in the western Fars (67 events between 51°E and 53.5°E), 85 % of the reverse and strike-slip earthquakes are nucleated above the Hormuz salt; and (3) the strike-slip earthquakes with foci in the basement, below the Hormuz salt, mostly occur associated with the Kazerun Fault (encircled focal depths).

A review on the historical earthquakes was provided by Gutiérrez et al. (2024). The most significant events include: (1) the May 4, 1853 Shiraz earthquake (I_o VIII) that caused the destruction of most of the city and killed 9000–11,000 people (Ambraseys and Melville, 1982; Berberian, 2014) and; (2) the 1972, M_S6.9 Qir (or Ghir) earthquake associated with the Surmeh Anticline east of the area covered by Fig. 2 (see western sector of meizoseismal zone). This major event killed more than 5010 people in a sparsely populated area and destroyed 50 villages. The environmental effects associated with this morphogenetic earthquake included secondary surface ruptures ascribed to flexural-slip faults, liquefaction and the occurrence of springs (Dewey and Grantz, 1973; Ambraseys and Melville, 1982; Berberian, 1995, 2014; Ambraseys and Jackson, 1998).

3. Methodology

Updated geological and geomorphological maps of the Jahani salt extrusion and the nearby area have been produced. Initially, a preliminary geological map was generated from the interpretation of greyscale aerial photographs from December 1994 (National Cartographic Centre of Iran, approximate scale of 1:44,000) with the aid of the available geological maps at 1:250,000 (Perry et al., 1965) and 1:100,000 scales (GSI, 1996, 2009). These initial geological maps were improved upon, using satellite images and high-resolution digital elevation models (DEMS). The final geological map was elaborated with ArcMap using satellite images (ESRI World Imagery, Google Earth) and a shaded relief model derived from TanDEM-X DEMs (12 m resolution; German Aerospace Center, DLR). Detailed geomorphological mapping was carried out in ArcMap using Google Earth satellite images with spatial resolution better than 2 m and hillshades. The TanDEM-X DEM was used to compute a number of parameters for the morphometric characterisation of the salt extrusion and the associated geomorphic features. These DEMs, derived from bistatic X-Band interferometric Synthetic Aperture Radar (SAR) data acquired by the satellites TanDEM-X (TDX) and TerraSAR-X (TSX), have absolute and relative vertical accuracies of <10 m and 2–4 cm, respectively (Wessel, 2016).

Three samples of fine-grained detrital deposits were collected for OSL dating (Optically Stimulated Luminescence), two of them (Ja-Fault-Up and Ja-Fault-Down) from a terrace deposit faulted by the Kareh Bas Fault, and another one (Ja-Lake2) from sediments deposited in a paleolake created when the Shur River was dammed by the northern namakier of the Jahani salt extrusion (Table 1, see location in Fig. 3). Samples for equivalent dose (D_E) analysis were taken by inserting light-proof PVC tubes in the selected layers. A bulk sediment sample was also collected from each sampling point for external dose rate (D) calculation. Detailed descriptions on the sampling and analytical protocols of the CENIEH Geochronological Laboratory can be found in Moreno et al. (2017, 2021).

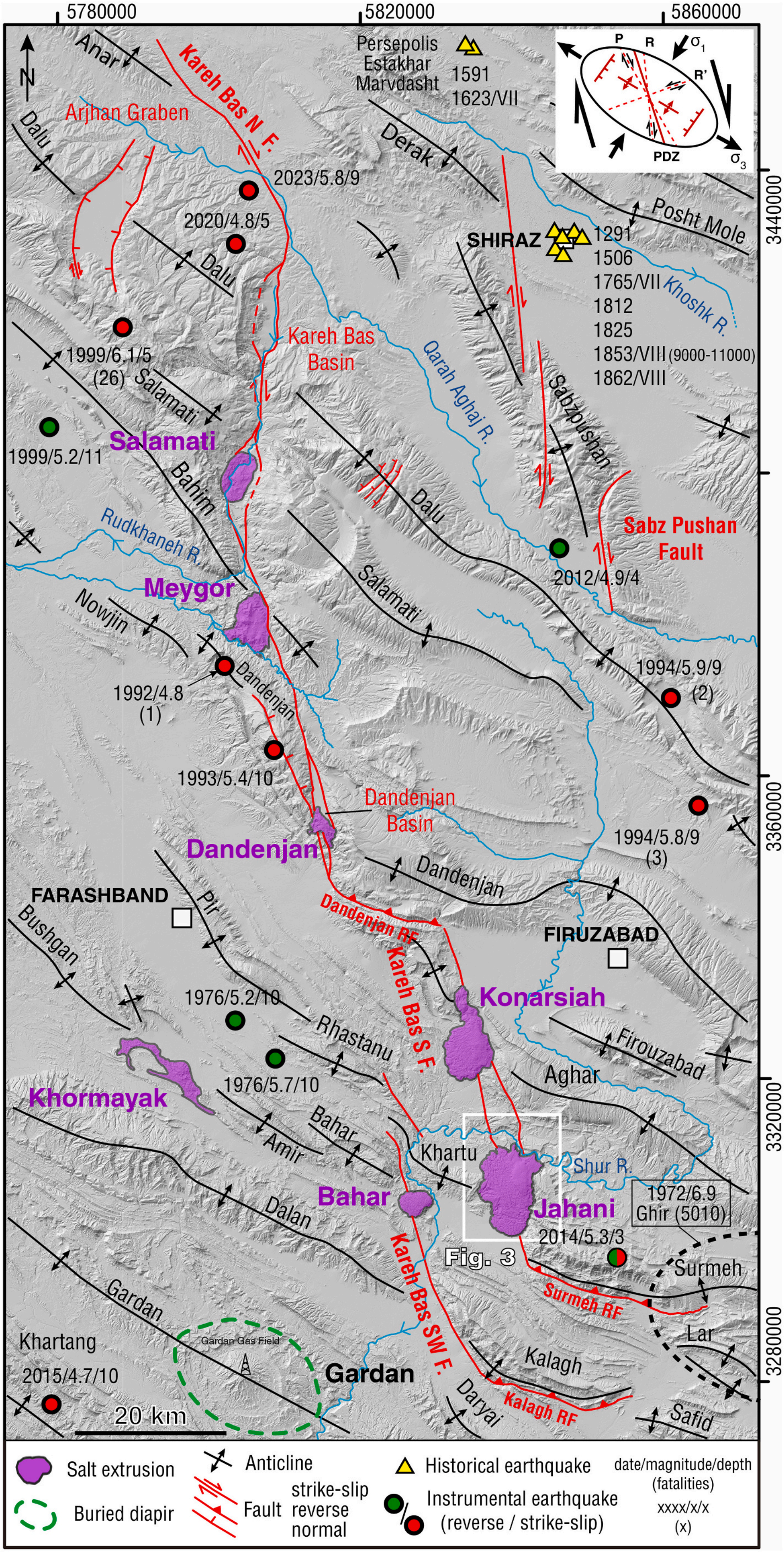

(caption on next page)

Fig. 2. Shaded relief model with the different geometric segments of the Kareh Bas fault system, the associated salt extrusions, and seismicity. Mapping of the Sabz Pushan fault system is based on Nezamzadeh et al. (2024). Historical earthquakes from the catalogs (10–1000 CE) of Ambraseys and Melville (1982) and Berberian (2014) are indicated with triangles, along with the year of occurrence and if available, the intensity from the Modified Mercalli scale. Most of the epicentres of the instrumental earthquakes are derived from the relocated earthquake catalog (1951–2018; location error <5 km) of Karasözen et al. (2019), differentiating the dominant style of faulting (red: strike-slip; green: reverse), and indicating their date, magnitude and calibrated focal depth (uncertainty <5 km). Earthquakes younger than 2018 are from the database of the Iranian Seismological Center. No moderate or large earthquakes were recorded in the area between 1890 and 1951 (Berberian, 2014). The black dashed line depicts the meizoseismal zone of the 1972 Ms 6.9 reverse fault Qir earthquake, with the epicentre located to the east of the map area. Number of fatalities caused by some earthquakes indicated in parenthesis. Inset shows strain ellipsoid associated with a virtual NNW-SSE right-lateral strike-slip fault. Green dashed line indicates a buried diapir and the associated gas field. See location of map area in Fig. 1 (Adapted from Gutiérrez et al., 2024).

Table 1
Summary table of OSL dating results on quartz grains including field, the calculated dose rates and the parameters used for computing dosimetry, the estimated equivalent dose (D_E), and the derived age expressed in kiloyears before present (ka). A 5 % error has been added to the estimated water content. Error margins are presented at 1-sigma. n/N: Number of aliquots that passed SAR acceptance criteria/total measured aliquots (outliers beyond 1.5 times the interquartile range have been removed); OD: Overdispersion; CAM: Central Age Model; D_E: Equivalent dose.

Field code	Ja-Fault-Up	Ja-Fault-Down	Ja-Lake2
Coordinates	39R 640463E 3171919N	39R 640464E 3171919N	39R 646853E 3170138N
Water content (%)	5	5	5
Depth (m)	3.4	4.3	16
238 U (ppm)	1.79 ± 0.05	1.88 ± 0.05	1.85 ± 0.05
232Th (ppm)	2.43 ± 0.09	2.97 ± 0.11	2.04 ± 0.08
87Rb (ppm)	18.4 ± 0.6	29.4 ± 0.9	14.03 ± 0.4
40K (%)	0.69 ± 0.01	1.14 ± 0.02	0.39 ± 0.01
Cosmic dose rate (Gy/ka)	0.15 ± 0.02	0.13 ± 0.01	0.047 ± 0.01
Dose rate (Gy/ka)	1.34 ± 0.05	1.80 ± 0.08	0.95 ± 0.04
Grain size (μm)	180–250	180–250	180–250
n/N	17/24	19/24	6/24
OD (%)	22	35	23
Age Model	CAM	CAM	CAM
DE (Gy)	17.9 ± 1.6	26.5 ± 2.9	26.4 ± 4.5
Age (ka)	13.4 ± 1.3	14.8 ± 1.7	27.68 ± 4.88

Luminescence measurements were carried out at the CENIEH Luminescence Laboratory in Burgos, Spain, using a Risø TL/OSL DA20 reader, equipped with bialkali EMI 9235QB15 photomultiplier tubes and a 90SR/90Y beta source (dose rate of ~0.10 Gy/s). Blue light (470 nm) was used for stimulation. Quartz grains of sizes 180–250 μm were mounted on stainless steel discs and fixed using a 2 mm patch of silicone oil. Quartz multi-grain aliquots were measured following the Single-Aliquot Regenerative-dose (SAR) protocol (Murray and Wintle, 2000, 2003) to obtain representative dose distributions. Details of the SAR protocol are given in Table S1 of the Supplementary data. Final D_E values were estimated following the Central Age Model (CAM; Galbraith et al., 1999; Duller, 2008). Environmental dose rates (D) were calculated as a contribution of beta, gamma and cosmic radiation, and were derived from radionuclide activity concentration determined by ICP-MS analysis and the following parameters: dose rate conversion factors (Guérin et al., 2011), alpha and beta grain size attenuation factors from Brennan et al. (1991) and Guérin et al. (2012), water content attenuation from Aitken and Xie (1990), and etching attenuation factors from Brennan (2003). Cosmic dose rate was calculated following Prescott and Hutton (1994) considering depth, altitude and longitude and latitude. A 5 % error has been added to the estimated water content used for the correction. Environmental dose rates to an infinite matrix values have been calculated using the Dose Rate & Age Calculator (DRAC, Durcan et al., 2015). Dose recovery preheat test results, OSL decay curves and dose response curves, and abanico plots of OSL D_E distributions are presented in Figs. S2, S3, S4, and S5 of Supplementary data.

Surface deformations were estimated from time-series analysis of the European Space Agency's (ESA) C-band SAR satellite Sentinel-1. Both ascending (track 28) and descending (track 137) observations were processed using the Small Baseline Subset (SBAS) technique (Berardino et al., 2002). The ascending data includes 199 images acquired between 13.11.2016 and 28.07.2023, while the descending data includes 200 images collected between 28.09.2015 and 24.07.2023. For each track, a network of small temporal baseline interferograms was generated using the Alaska Satellite Facility's Hybrid Pluggable Processing Pipeline (HyP3) system (Hogenson et al., 2020). The Copernicus GLO-30 Public DEM was employed by the HyP3 system for topographic phase removal and geocoding during InSAR processing. In total 948 and 875 interferograms were generated with the ascending and descending track data, respectively, and all interferograms had temporal baselines smaller than 120 days. As Sentinel-1 has a narrow orbital tube, which preserve interferometric coherence, no threshold was imposed on the perpendicular baseline. A multilooking factor of 2 in azimuth and 10 in range was applied to the interferograms. Before phase unwrapping, an adaptive filter with alpha = 0.6 was applied to the interferograms to reduce phase noise (Goldstein and Werner, 1998). The time series analysis was performed using the MintPy package (Yunjun et al., 2019). The network of interferograms was inverted using least squares to retrieve time series data (Berardino et al., 2002), and the topographic residual errors were estimated and subtracted from the time series (Fattahi and Amelung, 2013). A temporal coherence threshold of 0.9 was applied to mask out pixels with high noise level (Pepe and Lanari, 2006). The vertical and east-west deformation rates were estimated from the line-of-sight measurements in the two geometries neglecting the north component (Wright et al., 2004). The decomposition process considered sensor geometry, with an incidence angle of approximately 40° and a look angle azimuth of approximately 77° for ascending track, and an incidence angle of approximately 35° with a look angle azimuth of approximately 283° for descending track.

4. Results

4.1. *The geology associated with the Jahani salt extrusion*

The following cartographic units were differentiated in the geological map covering the Jahani salt extrusion and its vicinity (Fig. 3): (1) the extruded Neoproterozoic-Cambrian age Hormuz Group, consisting of a thick halite-dominated evaporitic succession with intercalated units of non-evaporitic rocks; (2) a Jurassic-Cretaceous succession dominated by carbonate rocks including the Khami and Bangestan groups; (3) Late Cretaceous marls of the Gurpi Fm. and Paleogene shales of the Pabdeh Fm.; (4) the cliff-forming Oligocene-Early Miocene Asmari Limestone; (5) marls, gypsum and interbedded limestone of the Miocene Gachsaran Fm.; (6) the Miocene-age Mishan Fm., consisting of a basal limestone unit (Guri Mb.) and a thick succession of greenish marls with an additional limestone unit intercalated in the upper part, designated as the Garulizak Mb.; and (7) the unconformable Plio-Quaternary conglomerates of the Bakhtyari Fm.

The Hormuz salt extruded at Jahani displays intercalations of non-evaporitic reddish rocks with an overall concentric distribution with respect to both the flanks of the summit dome and the distal front of the salt fountain (Fig. 3). The outermost intercalation is a laterally continuous, ridge-forming unit, consisting of red limestones and marls with a conformable breccia of black dolostone veined with sphalerite. This is a subvertical to overturned bed with inward centripetal dip showing an overall funnel-shaped geometry (Kent, 1958; Talbot and Alavi, 1996;

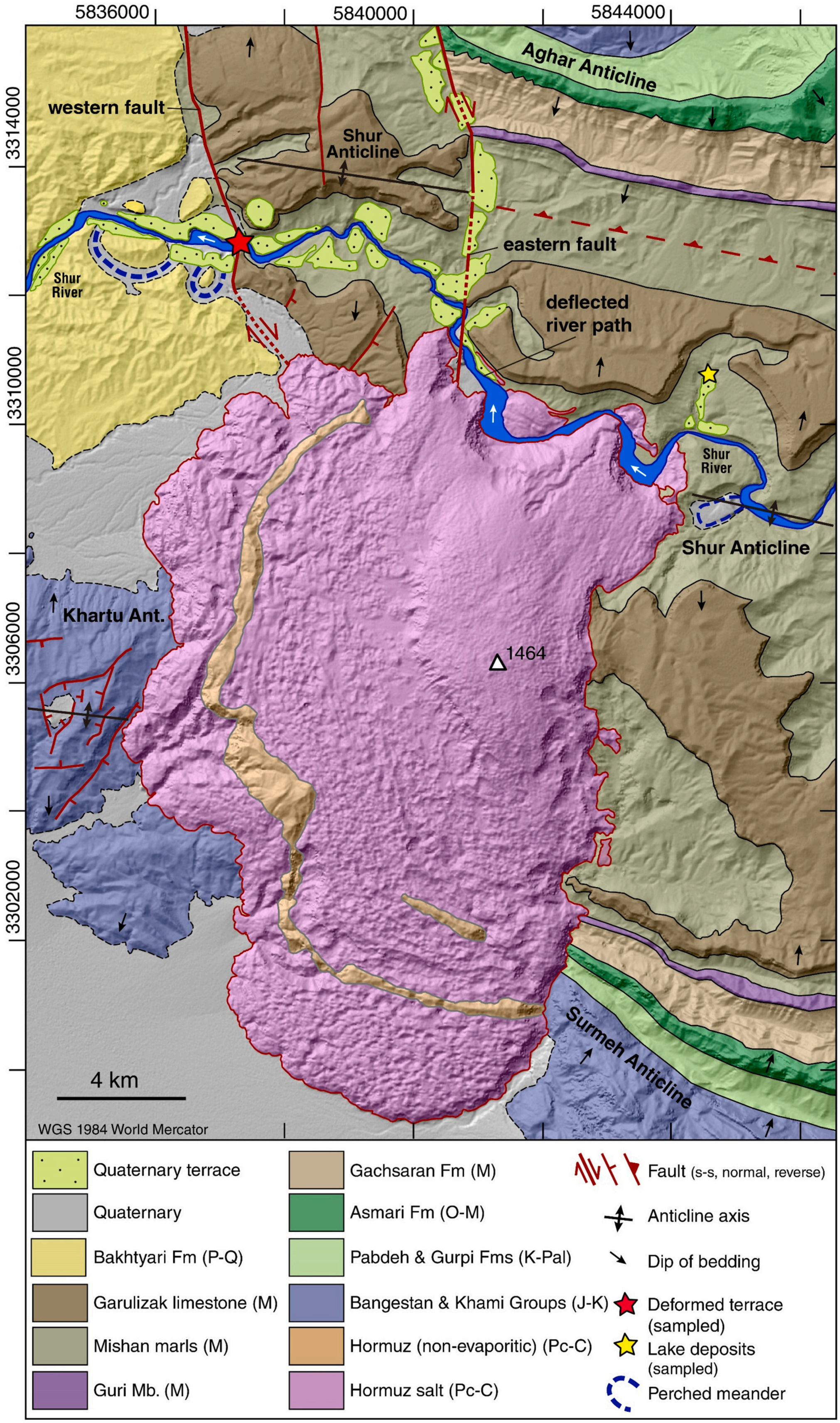

Fig. 3. Geological map of Jahani salt extrusion (red polygon) and its vicinity, associated with two overlapping strands (western and eastern) of the Kareh Bas Fault and the west-flowing Shur River. The age of the cartographic units is indicated with letters in the legend; Q: Quaternary, P: Pliocene, M: Miocene, O: Oligocene, Pal: Paleogene, K: Cretaceous, J: Jurassic, C: Cambrian, Pc: Precambrian (Neoproterozoic). See location of map area in Fig. 2.

Talbot et al., 2000; Tayebi et al., 2013). These strata might correspond to the steeply dipping lower limb of an outward verging secondary fold developed in the upper limb of the first-order recumbent fold characteristic of subaerial salt sheets (Talbot, 1979; Talbot and Aftabi, 2004; Jackson and Hudec, 2017). In the southern namakier there is another ridge-forming intercalation of non-evaporitic rocks with limited extent situated around 900 m to the north (Fig. 3). The rest of the intercalations are discontinuous, rather thin and with subdued geomorphic expression. Talbot and Alavi (1996) and Talbot et al. (2000) proposed the differentiation of two units in the Hormuz Group separated by the outer red intercalation exposed in Jahani and of presumed Cambrian age: (1) an inner older succession (Neoproterozoic component) of thick bedded multi-coloured halite interbedded with anhydrite, dark foetid dolomites and other subordinate lithologies (sandstones, siltstones, marls, orthoquartzites); and (2) a younger succession (Cambrian component) in the outer fringe of the salt fountain dominated by grey and bluff halite with dispersed anhydrite and volcanic inclusions. The overall distribution of the units suggests that the younger salt unit (Cambrian?) extruded first and was overturned and overridden by the older unit (Neoproterozoic?), with some potential decoupling between the salt units and the more competent intervening non-evaporitic bed. Talbot et al. (2000) interpreted the discontinuous intercalations of non-evaporitic red beds with concentric distribution as thrust repetitions of the unit corresponding to the outer intercalation. Jackson and Hudec (2017) suggested that the red concentric bands could correspond to Neogene residual soils (surficial dissolution residues) that record alternating phases of weathering followed by episodes of resurgent salt flow, during which the newly spelled salt would override the soil developed atop a previously wasted salt glacier. This interpretation, implicitly involving episodic salt extrusion, suggests that the red bands correspond to regoliths of different ages that separate salt extruded in different surges following a piggy-back sequence. However, field observations indicate that these red bands are Hormuz-age bedrock units clearly interbedded within the salt, rather than recent weathering deposits.

The geological structure in the study area is characterised by NW-SE to WNW-ESE trending folds with relatively sinuous axes, offset by the right-lateral Kareh Bas strike-slip fault system (Talbot and Alavi, 1996; Jahani et al., 2017; Hassanpour et al., 2018). Here, the southern segment of the Kareh Bas fault comprises two strands with a right-stepping arrangement, designated as the western and eastern faults (Figs. 2, 3). The releasing stepover overlaps between the Konarsiah and Jahani salt extrusions. The latter occurs associated with the northern termination of the western fault and the southern termination of the eastern fault, respectively. The separation of the two fault strands in the overlapping zone between Konarsiah and Jahani diapirs ranges between 1.7 and 4 km. The overlapping section, partially concealed by the salt extrusions, has a minimum length of 9 km.

The 32 km long and NNW-SSE oriented eastern fault extends from the Dandenjan reverse fault to the Jahani Diapir, and controls the relatively straight eastern margin of the Konarsiah salt extrusion (Fig. 2). Zarei et al. (2012) interpreted that the elongated Konarsiah salt extrusion is a waning salt fountain linked to two vents pulled apart between two strands of the Kareh Bas Fault (or Mengarak Fault). The eastern fault offsets dextrally 4.5–5 km the axis of the Aghar Anticline, which shows deflections in the vicinity of the fault and the diapir (Figs. 2, 3). These local changes in the fold trend can be related to changes in the propagation path of the anticlines controlled by the presence of weak precursor diapirs acting as strain localizers (deflection on western side) (Callot et al., 2007; Jahani et al., 2009), and to ductile shear associated with the fault displacement (deflection of strata on eastern side).

The 50 km long western fault curves eastward south of the Jahani salt extrusion connecting with the Surmeh reverse fault, at the southern overturned limb of the asymmetric Surmeh Anticline (Fig. 2). The Surmeh Anticline overrides Plio-Quaternary Bakhtyari conglomerates (Perry et al., 1965; GSI, 1996) along the Surmeh reverse fault, and it is the only locality within the Simply Folded Belt where Paleozoic rocks (Ordovician and younger) are exposed (Berberian, 1995; GSI, 1996). Here, uplift results from the contribution of folding plus reverse faulting at the contractional bend. The western fault strand offsets right-laterally 5–5.5 km the axis of the Khartu-Surmeh Anticline (Fig. 2). Just west of the Jahani salt extrusion, the exposures of the upper part of the Bangestan Group (Cretaceous Sarvak limestone) in the crestal zone of the Khartu Anticline display conspicuous depressions with a local relief of around 50 m associated with downthrown blocks controlled by polygonal normal faults (Fig. 3). The longitudinal normal faults in the inflection zone between the fold crest and northern limb are expressed as scarps with wide-open and fresh-looking fissures. The strong disruption of the fold, restricted to the vicinity of the diapir, could be ascribed to salt withdrawal form the core of the anticline and/or enhanced moment-bending faulting related to buckle folding in the vicinity of the diapir.

To the west of the Jahani salt extrusion, between the Aghar Anticline and the Surmeh Anticline there is broad synclinorium (Dehrood Syncline in GSI, 1996) with a secondary open anticline, here designated as the Shur Anticline (Fig. 3). This fold is clearly recognizable thanks to the cuesta landforms with opposing slopes developed on the resistant Garulizak limestone (caprock). The axis of this anticline is offset horizontally 3.9 km along the eastern fault. In the sector between the overlapping eastern and western faults, the backslope of the cuesta developed on S-dipping Garulizak limestone (southern anticline limb) displays two conspicuous scarps controlled by down-to-the-southeast, NE-SW oriented normal faults. These extensional structures are consistent with transtension in a releasing stepover associated with NNW-SSE trending dextral strike-slip faults (see strain ellipsoid in Fig. 2, with NW-SE-oriented σ3).

4.2. Quaternary deformation associated with the Kareh Bas strike-slip fault

No fully conclusive evidence of Quaternary faulting has been identified along the eastern strand of the Kareh Bas Fault. The deeply entrenched Shur River flows along the axis of the Shur Anticline upstream of the fault (i.e., valley-centred anticline), while downstream it flows along the southern limb of the anticline. At the fault trace, the Shur River shows a sharp deflection compatible with the right-lateral movement of the fault, despite the northern namakier of Jahani forces the upstream section of the river to migrate northwards, in a direction opposite to the sense of fault displacement (Fig. 3). The deflected path of the river suggests a potential horizontal deflection of ≥1.3 km. The eastern fault controls the path of a transverse tributary drainage on the northern margin of the Shur River. Upstream of the ridge formed by Guri limestone, the eastern side of the valley and the associated terraces display a rectilinear boundary suggesting a steep fault contact between the bedrock and the Quaternary alluvium. An outcrop associated with the ridge of Guri limestone displays a vertical contact between limestone on the eastern side and massive bouldery alluvium and colluvium on the western side (39R 643435E 3173444N). The contact seems to correspond to a vertical fault plane that has affected the Quaternary gravels and dragged limestone strata to an attitude parallel to the fault (Fig. S1 in Supplementary data). However, no clear offset or shear fabrics can be observed in the coarse and massive gravels. Within the exposed gravels of the terrace deposit, a vertical contact between boulders and gravels with different size and textural features, together with some elongated clasts showing subvertical fabrics, suggest the presence of a fault. However, the massive and bouldery nature of the alluvium precludes unambiguously ascribing the steep contact to a fault (Fig. S1 in Supplementary data).

Gutiérrez et al. (2024) documented that the western fault has deformed a terrace deposit of the W-flowing Shur River, which aggradation surface lies 40 m above the current channel (39R 640463E 3171919N). The outcrop on the northern valley margin shows a steep fault plane with down-to-the-E displacement component and three packages in the terrace deposits differentiated based on the degree of deformation (Fig. 4). The lower one, restricted to the downthrown upstream block corresponds to faulted gravels with an abrupt downward bend close to the fault (Fig. 4A). An intermediate package, well exposed in an E-W-oriented road cutting and that extends across the trace of the fault, displays a synformal structure (Fig. 4B). The gravel beds on the western limb dip upstream and the core on the synform is filled by well-sorted sand facies 2.7–4 m thick. The 2.4 m thick upper package corresponds to the laterally continuous and non-deformed uppermost unit of the terrace deposit (Fig. 4B).

Two samples were collected for OSL dating from the sand-filled synformal trough exposed in the road cut, which shows two channel-shaped units and gravel beds that pinch out in the downstream direction (Fig. 4A). The samples collected from the lower (western) and the higher (eastern) channels have yielded consistent OSL ages of 14.8 ± 1.7 ka and 13.4 ± 1.3 ka, respectively (Fig. 4B; Table 1). The two ages overlap at 14.7–13.8 ka, indicating the age of the sands filling the core of the synformal trough were most likely deposited in a very short time period. The stratigraphic and structural relationships allow us to infer a minimum of two surface faulting or folding events occurred during the accumulation of the terrace deposit. The oldest one occurred before 14.7–13.8 ka and ruptured the lower gravel package. A younger meter-scale displacement event folded the gravels of the intermediate package, generating a transverse, fault-parallel trough subsequently filled by sand facies. The OSL age of 14.7–13.8 ka obtained for the sand fill of the trough, deposited soon after the surface deformation event, can be considered as a good estimate for the timing of the youngest paleo-earthquake. The fact that the upper gravel package does not show any evidence of deformation suggests that this corresponds to the most recent surface-deforming event (MRE) on the western strand of the Kareh Bas fault at this site.

Just downstream of the western fault, the southern margin of the Shur River exhibits two perched incised meander cutoffs carved into Bakhtyari conglomerates at around 45 m above the current thalweg (Fig. 3). These landforms are consistent with the down-to-the-east vertical displacement of the fault, which tends to attenuate or even reverse the gradient of the river channel. The fluvial system can counterbalance the effect of this deformation by increasing the incision rate and straightening the channel by meander cut-off in the upthrown block (Harvey, 2007).

4.3. *General geomorphology of the Jahani salt extrusion*

At the present time, the Jahani salt fountain covers an area of 67.9 km^2 and reaches a maximum local relief of 918 m between the highest point of the summit dome (1464 m a.s.l.) and the lowest point of the southern namakier front (Figs. 5, 6). Gutiérrez et al. (2024) estimated a maximum volume for the extrusion of 10,699 Mm^3 computing the volume of the 3D space enclosed by two TIN surfaces corresponding to the topography of the salt fountain and a basal surface interpolated from its perimeter. The construction of cross-sections considering the location of the vent underlying the summit dome, and that the namakiers thin towards their front, suggests that the actual volume of the salt fountain could be around 80 % of the maximum estimate (i.e., ca. 8500 Mm^3). This figure yields a volume/area ratio of 125 m, which provides a rough estimate for the average thickness of Hormuz rocks in the salt fountain. The salt extrusion shows an elongated geometry with a major N-S-

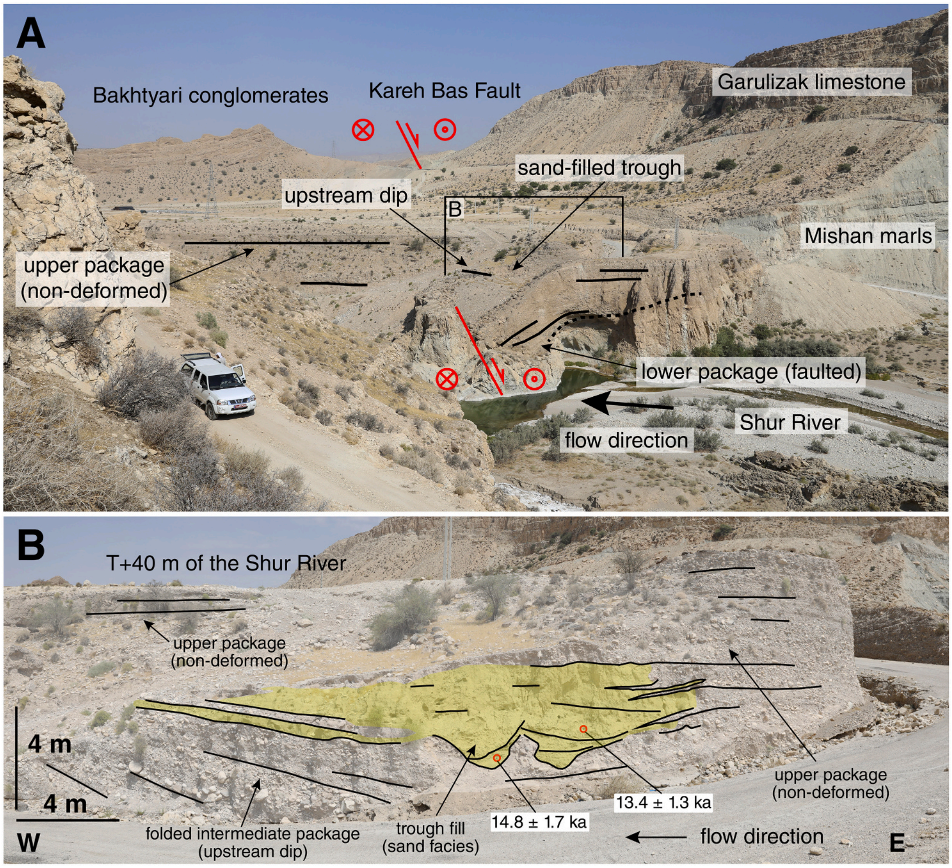

Fig. 4. Terrace on the northern margin of the Shur River deformed by episodic displacement on the western strand of the Kerah Bas Fault. Location marked with a red star in Fig. 3. A: Exposure of the fault with down-to-the-E displacement that offset bent gravels at the base of the terrace deposit. B: Sand-filled trough associated with folded gravels recording the most recent surface-deformation event. Note gravel on the western limb of the synform dipping upstream and non-deformed gravels at the top of the sequence. Samples collected from sand-filled trough and the estimated OSL ages are indicated. See text for further explanation (Adapted from Gutiérrez et al., 2024).

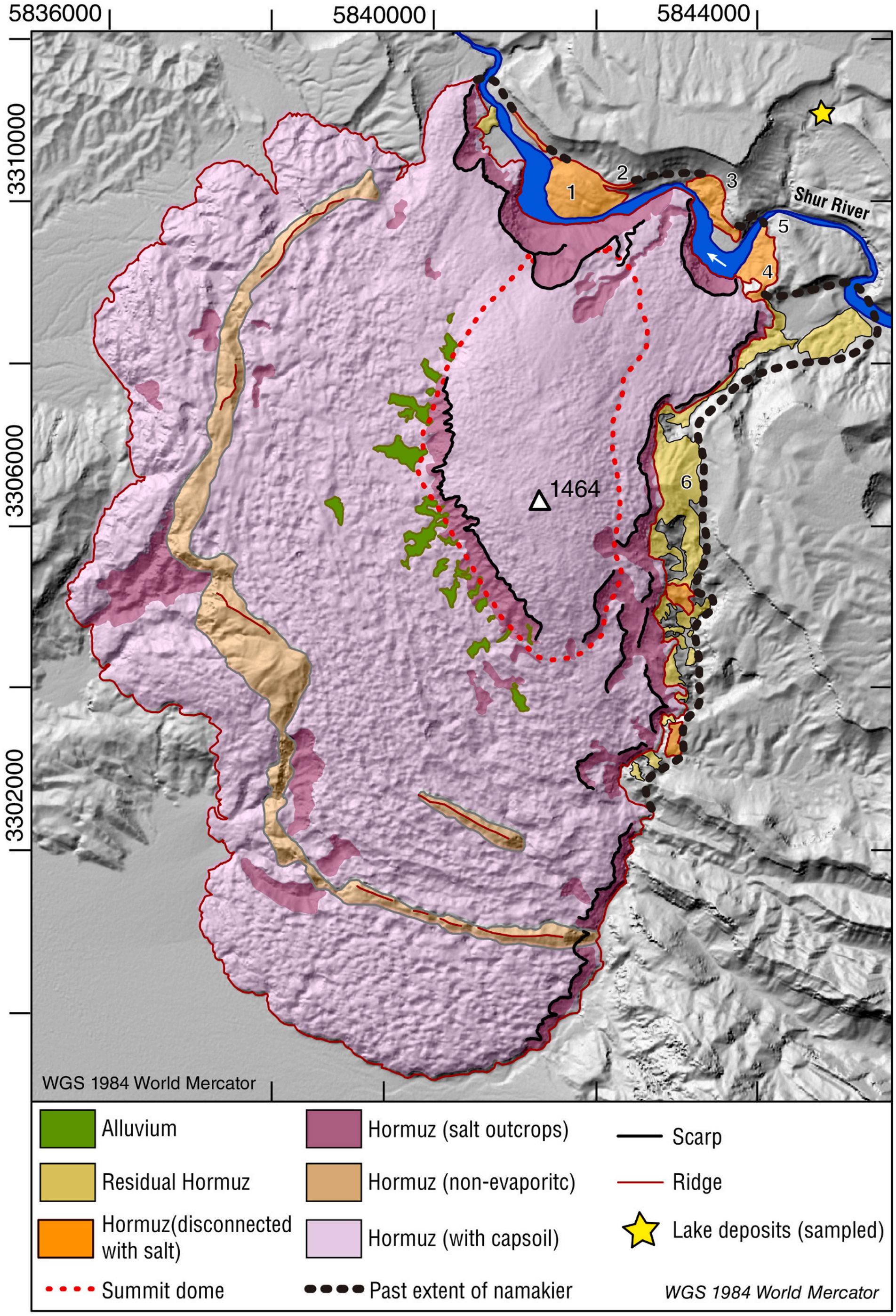

Fig. 5. Geomorphological map of the Jahani salt extrusion, showing the maximum extent reached in the past when the northern namakier blocked the Shur River. The former outline of the salt fountain has been reconstructed on the basis of disconnected masses of salt-bearing Hormuz and Hormuz-derived residual deposits. Numbers refer to specific locations described in the text.

oriented axis 12.35 km long, roughly parallel to the Kareh Bas Fault, and a minor E-W axis 7.37 km in length. The summit dome, protruding around 250 m above the surrounding namakiers covers an area of 9.4 km^2 (ca. 14 % of the salt fountain). It has an eccentric position on the northeastern sector of the extrusion, and also displays a N-S-oriented geometry, 5 km long and 2.5 km wide (Fig. 5). Its flanks are expressed by steep slopes and well-defined slope breaks at the junction with the salt glaciers (Fig. 6A). The steep sides of the summit dome mostly correspond to salt outcrops dissected by dense gully networks (Figs. 5, 6A). In these steep slopes the residual material derived from salt dissolution is rapidly eroded, preventing the development of the capsoils and sinkholes that dominate the rest of the salt extrusion (Bruthans et al., 2008, 2009, 2017; Zarei et al., 2012; Abirifard et al., 2017). The location of the summit dome and its asymmetric morphology in plan, with E-facing convexity, reflect the location of the elongated vent through which the salt rises, and the presence of confining high-topography to the east of the vent (i.e., high cuesta capped by S-dipping Garulizak limestones) (Figs. 5, 8). On the northern sector the summit dome is scalloped by a salt escarpment up to 425 m high associated with the sinuous Shur River (Figs. 5, 6F).

The salt flows radially from the summit dome virtually in all directions except to the east, where the high reliefs at the southern limb of

Fig. 6. Images illustrating different geomorphic domains of the Jahani salt extrusion. A: Summit dome (SD) with steep bare and densely dissected salt slopes in the flanks affected by a landslide scar (LS) and an alluviated internally-drained depression (AD) at the proximal sector of the western namakier (WN). B: Southern lobe superposed on the southern piedmont, looking to the east. Reddish rocks correspond to the non-evaporitic unit (NEU) intercalated within the Hormuz series. Surmeh and Khartu anticlines (SA, KA) in the background and foreground, respectively. C: Closer view of the frontal zone of the southern lobe, looking to the west. Tent of nomadic shepherds in the foreground. D: Eastern flank of the southern lobe, over-steepened by fluvial undermining (view to the north). Surmeh Anticline (SA) on the right. E: Steep and densely dissected bare salt slopes on the eastern flank of the southern lobe with brine spring (S). Circle indicates person for scale. F: Northern namakier dissected by the Shur River (SR). Disconnected salt-bearing Hormuz rocks on the left and salt escarpment on the right. Dashed line indicates maximum extent of northern namakier (AA: Aghar Anticine; GL: cuesta capped by Garulizak limestone; SA: Shur Anticline). G: Large salt quarry in the SW-directed lobe, with two intercalated non-evaporitic units (NEU).

the Shur Anticline and the Surmeh anticlinal ridge exert a confining effect (Fig. 5). The west- and south-flowing namakiers, unaffected by erosion along their distal sector, have general slopes within the range of 6.6–7.5°. Different lobes can be differentiated in the distal sector of the spreading salt sheet guided by erosional gaps. The southern lobe, 5.4 km long and 5.2 km wide, overrides an extensive alluvial piedmont between the dextrally offset Khartu and Surmeh anticlines (Fig. 6B, C). The eastern side of this lobe is over-steepened by a undermining related to a lateral drainage that prevents its eastward expansion and results in the development of a densely gullied bare-salt escarpment (Fig. 6D, E). The SW-directed lobe 3.2 km wide penetrates through a gap in the collapsed Khartu Anticline. The rather dissected front of the NW-directed lobe, 4.8 km wide, advances over a piedmont between the Khartu and Shur anticlines. The frontal sector of the S-, SW- and NW-directed lobes do not show any evidence of retreat, typically expressed by residual Hormuz deposits or less weathered bedrock surfaces. The 4 km wide northern lobe cascades into the deeply entrenched Shur River, which has trimmed the namakier forming a salt escarpment up to 425 m high. This escarpment, with a cartographic length of around 6 km, shows a sinuous trace controlled by the meandering pattern of the Shur River, with the highest and steepest sections associated with the outer side of meanders (Gutiérrez et al., 2025) (Figs. 5, 6F).

With the exception of the outcrops of non-evaporitic Hormuz rocks (Fig. 6G) and the steep salt escarpments, the salt extrusion is most covered by capsoil (dissolution residue) and riddled by densely packed sinkholes. Salt exposures represent 10.2 % of the total area (Gutiérrez et al., 2025). Gutiérrez et al. (2025) analysed the morphometry of sinkholes in the southern salt glacier, showing a morpho-chronological gradation, and mapped alluviated poljes at the foot of the western flank of the summit dome (Figs. 5, 6A).

4.4. Damming of the Shur River by the northern salt glacier

Along the northern and eastern margins of the Jahani salt extrusion there are remnants of Hormuz rocks with distinctive reddish and grey colors indicating that the namakiers in those sectors reached a greater extent in the past (Figs. 6A, 7, 8). The map in Fig. 5 differentiates: (1) thick masses of Hormuz disconnected from the salt fountain with numerous fresh-looking sinkholes and observable outcrops of salt remnants; and (2) relatively thin deposits of residual Hormuz with smooth topography that drape the countryrock and lack sinkholes. The reconstruction of the maximum extent of the salt fountain on the basis of these units reveals that sometime in the past the northern namakier blocked the Shur River along a 6 km long section and surmounted the northern valley margin. The larger mass of Hormuz disconnected from the salt fountain occurs in the inner side of a meander of the Shur River (label as 1 in Fig. 5, Fig. 7A). This mass rises 90 m above the river channel and displays a valley-parallel ridge and trough topography stepping towards the river. This overall morphology is likely related to the compressional flow that operated when the front of the glacier reached the valley margin, acting as a backstop, and subsequently modified by gravitational deformation and salt dissolution-induced subsidence. This body of disconnected Hormuz is riddled by fresh-looking sinkholes, some showing salt exposures on their steep walls, while the valley side displays a ridge of residual Hormuz dissected by gullies and lacking sinkholes. This portion could correspond to a "push moraine" developed when the advance of the salt glacier bulldozed deposits related to a previous damming event. The continuation of the Hormuz to the west (i.e., downstream) is expressed as a bouldery moraine-like ridge along the valley margin. This ridge seems to represent a remnant of the distal edge

Fig. 7. Images of Hormuz masses disconnected from the salt fountain and residual Hormuz-derived deposits recording the maximum extent of the salt fountain (white dashed line in B, C and D) and the damming of the Shur River. A: Hill on the northern side of the Shur valley underlain by salt-bearing Hormuz and riddled by sinkholes (DH; labelled as 1 in Fig. 5). Thick colluvium (TC) and deflected drainage in the associated slope. To the left, moraine-like ridge (MR) of Hormuz marking the maximum extent of the namakier. In the background, the summit dome (SD) and northern namakier trimmed by a salt escarpment (SE) with hanging valleys (HV). B: Moraine-like ridge of residual Hormuz recording the maximum advance of the northern namakier (labelled as 2 in Fig. 5). Thick colluvium related to impeded runoff in the associated slope above. In the foreground, disconnected Hormuz (DH) with salt outcrops (SO). GL: Garulizak limestone; MM: Mishan marls. C: Disconnected mass of Hormuz associated with the outer side of a meander of the Shur River (SR) (labelled as 3 in Fig. 5). The Hormuz body, over-steepened by fluvial undermining, is affected by fresh landslides. Yellow dashed line indicate the landslide scars. D: Northeastern namakier lobe that grades into residual Hormuz deposits (labelled as 4 in Fig. 5), marking the maximum extent of the salt glacier (dashed line). The damming site (DS) is located to the left of a moraine-like accumulation of disconnected Hormuz. GL: Garulizak limestone; MM: Mishan marls. E: Canyon-like section of the Shur River valley (SR) where the drainage was blocked (i.e., upstream edge of namakier dam) (labelled as 5 in Fig. 5). Left side of the image, a moraine-like accumulation of Hormuz accumulated at the former namakier terminus (dashed line).

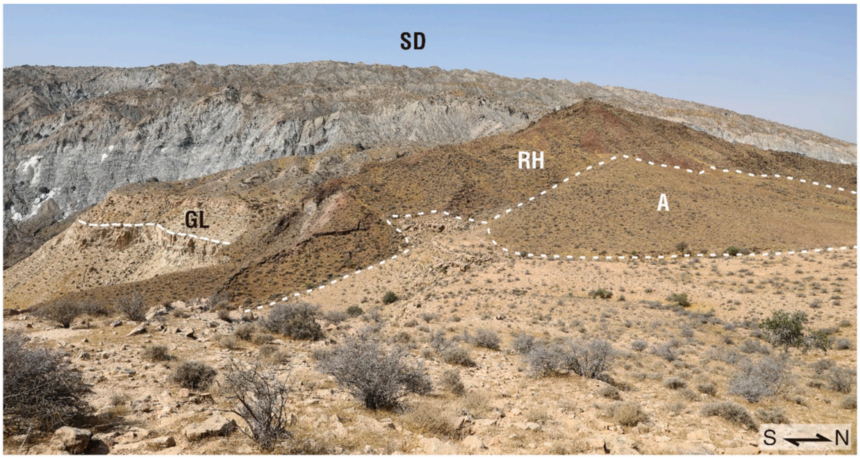

Fig. 8. Moraine-like accumulation of residual Hormuz (RH) on subhorizontal Garulizak limestone (GL; bedding marked with dashed lone) to the east of the summit dome (SD) (labelled as 6 in Fig. 5). At the foot of the ridge, colluvial apron (A) derived from the erosion of residual Hormuz.

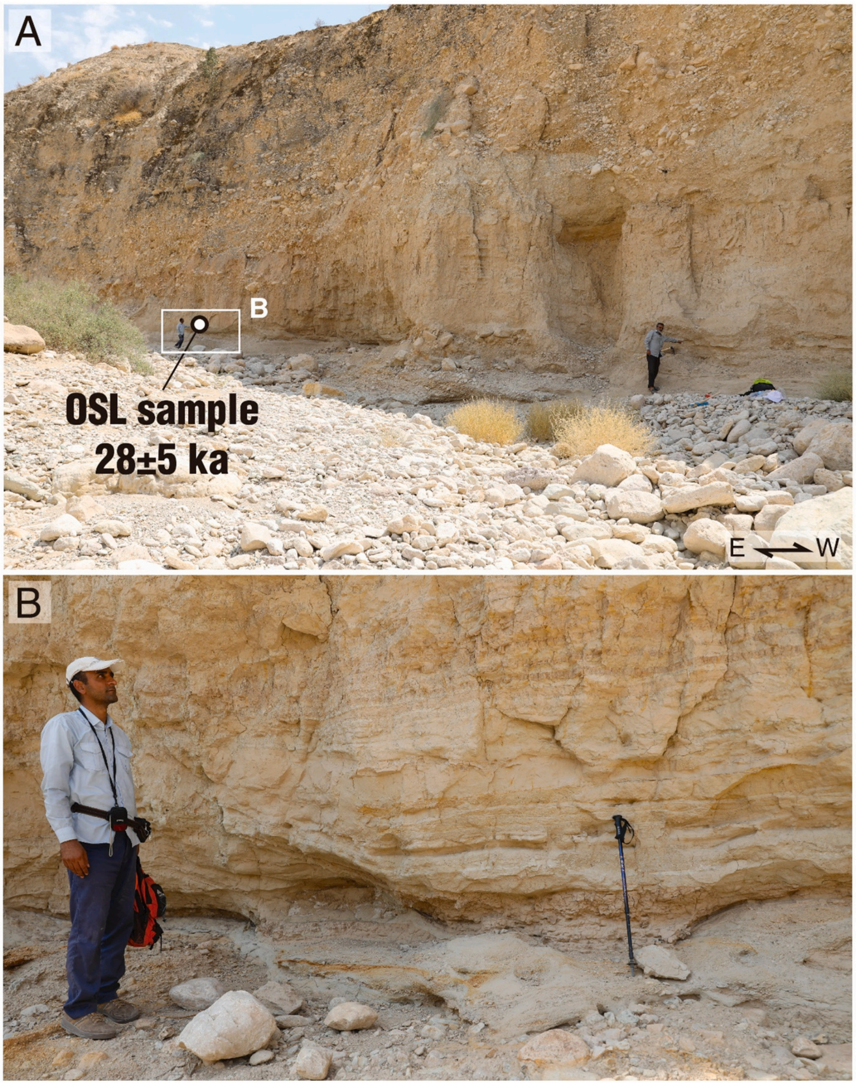

Fig. 9. Images of the exposure of paleolake deposits related to the damming of the Shur River by the northern namakier of the Jahani salt extrusion (location indicated with yellow star in Figs. 3 and 5). A: General view of the exposure. Person on the right points to the position of a sample of putative charcoal that did not contain any charred material. Person on the left marks the position of an OSL sample (Ja-Lake2) that yielded an age of 28 ± 5 ka. B: Close view of thinly-stratified and well-sorted fine-grained lacustrine deposits.

of the namakier that remains after significant fluvial erosion. To the east (i.e., upstream), the disconnected Hormuz continues as a moraine-like ridge perched 80 m above the river channel (labelled as 2 in Fig. 5, Fig. 7B). The slopes at the valley margin situated above the ridge display anomalously thick colluvium and deflected gullies related to the blockage of the local runoff by the namakier that surmounted the valley margin. Upstream, there is another large mass of disconnected Hormuz associated with the outer bend of a meander (labelled as 3 in Fig. 5, Fig. 7C). The Hormuz embedded to the valley margin reaches 120 m above the river channel and has largely collapsed by slope movements, as revealed by fresh-looking landslide scars. On the southern valley margin, the northern namakier grades distally into a relatively thin mantle of residual Hormuz that remains after the dissolution of the salt (labelled as 4 in Fig. 5, Fig. 7D). In this sector the distribution of the residual Hormuz reveals that an E-directed lobe developed in the past, with the potential of damming the Shur River (Fig. 5). The main damming site is situated in a narrow canyon-like section of the Shur River. Here, a moraine-like mass of disconnected Hormuz occurs on the southern side of the valley (labelled as 5 in Fig. 5, Fig. 7E).

Along the eastern margin of the salt fountain the bedrock is mantled by rather continuous deposits of residual Hormuz, indicating that the extrusion reached a greater extent to the east (Fig. 5). The eastward expansion of the salt fountain most probably occurred when the advance of the northern namakier was hindered by the opposite margin of the Shur valley, acting as a backstop. At this stage, a wave of compressional flow propagated upwards towards the summit dome inducing the local built up and expansion of the salt fountain. Anomalously thick residual Hormuz expressed as a reddish pointed hill occurs in the highest and relatively flat ground to the east of the summit dome (labelled as 6 in Fig. 5, Fig. 8). Initially, we thought that this flatiron-like hill might correspond to a flap of upturned bedrock strata. However, close field examination revealed that it corresponds to residual Hormuz underlain by subhorizontal Garulizak limestone. The high thickness of the residual Hormuz deposits at this site could be related to former quasi-stagnant salt in a nearly flat area and higher preservation in a low-gradient environment.

The initial hypothesis whereby the damming of the Shur River by the northern namakier of the Jahani salt extrusion created a lake upstream was corroborated by the identification of lacustrine deposits in a tributary drainage situated on the northern margin of the Shur Valley, just upstream of the damming site (Figs. 5 and 9). To our knowledge, this the first work that documents the blockage of a major drainage by a salt glacier and the creation of a namakier-dammed lake. The presence of old landslide dams in the small catchment where the deposits were found can be unambiguously ruled out, thanks to good exposure conditions of the well-bedded Mishan marls with interstratified limestone. The lacustrine deposits are exposed at the bank of a drainage in an exposure that extends for about 70 m and reaching a minimum of 6.1 m in thickness (base unexposed). It consists of tabular and well-stratified centimeter- to decimeter-scale beds of well-sorted and indurated silts, sands, clays and granule gravel, with some channels of pebble gravel. The lacustrine sediments are overlain by bouldery gravels that likely record alluvial sedimentation after the opening of the namakier dam and the disappearance of the lake. A sample of dark material with the appearance of charcoal was collected for radiocarbon dating, but examination at Beta Analytic indicated the lack of charred material. Another sample was collected from a sandy silt bed 2.9 m below the top of the lake deposit for OSL dating (Ja-Lake2) that provided an age of 28 ± 5 ka (Table 1). Unfortunately, the sample yielded poor luminescence results because of two factors: (1) the amount of quartz was very low (<0.20 g) and insufficient to measure over 24 aliquots; and (2) only 6 out of 24 measured aliquots met acceptance criteria. Therefore, this

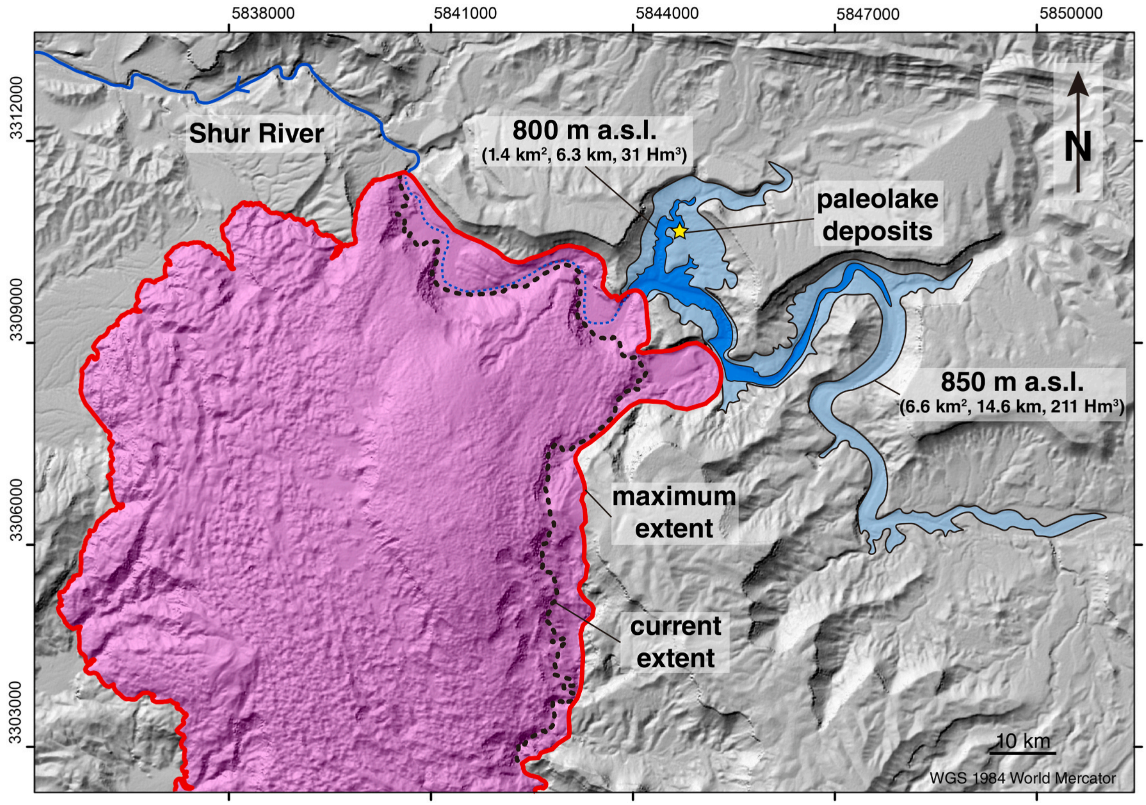

Fig. 10. Paleogeographic reconstruction of the paleolake created by the damming of the Shur River by the northern namakier of the Jahani salt extrusion, considering two water-level scenarios: (1) minimum elevation of 800 m given by the elevation of the paleolake deposits; and (2) maximum elevation of 850 m dictated by the lowest point of the highest namakier dam section. The parameters calculated for each scenario assume a topography similar to that at the present time.

result should be considered with caution (see Fig. S5 and Table S2 in Supplementary data).

A tentative paleogeographic reconstruction of the namakier-dammed lake has been produced considering two scenarios (Fig. 10): (1) a minimum water level at 800 m a.s.l., roughly corresponding to the elevation of the top of the lacustrine deposits; and (2) a maximum water level at 850 m a.s.l. given by the elevation of the saddle between the northern valley margin and the disconnected mass of Hormuz that reaches the highest altitude (site 3 labelled in Fig. 5). Assuming that the topography was similar to that at the present time, the 800 m contour indicates that the lake reached at least a depth 65 m at the damming site, an area of 1.4 km^2, a length along the sinuous valley axis of 6.3 km and a

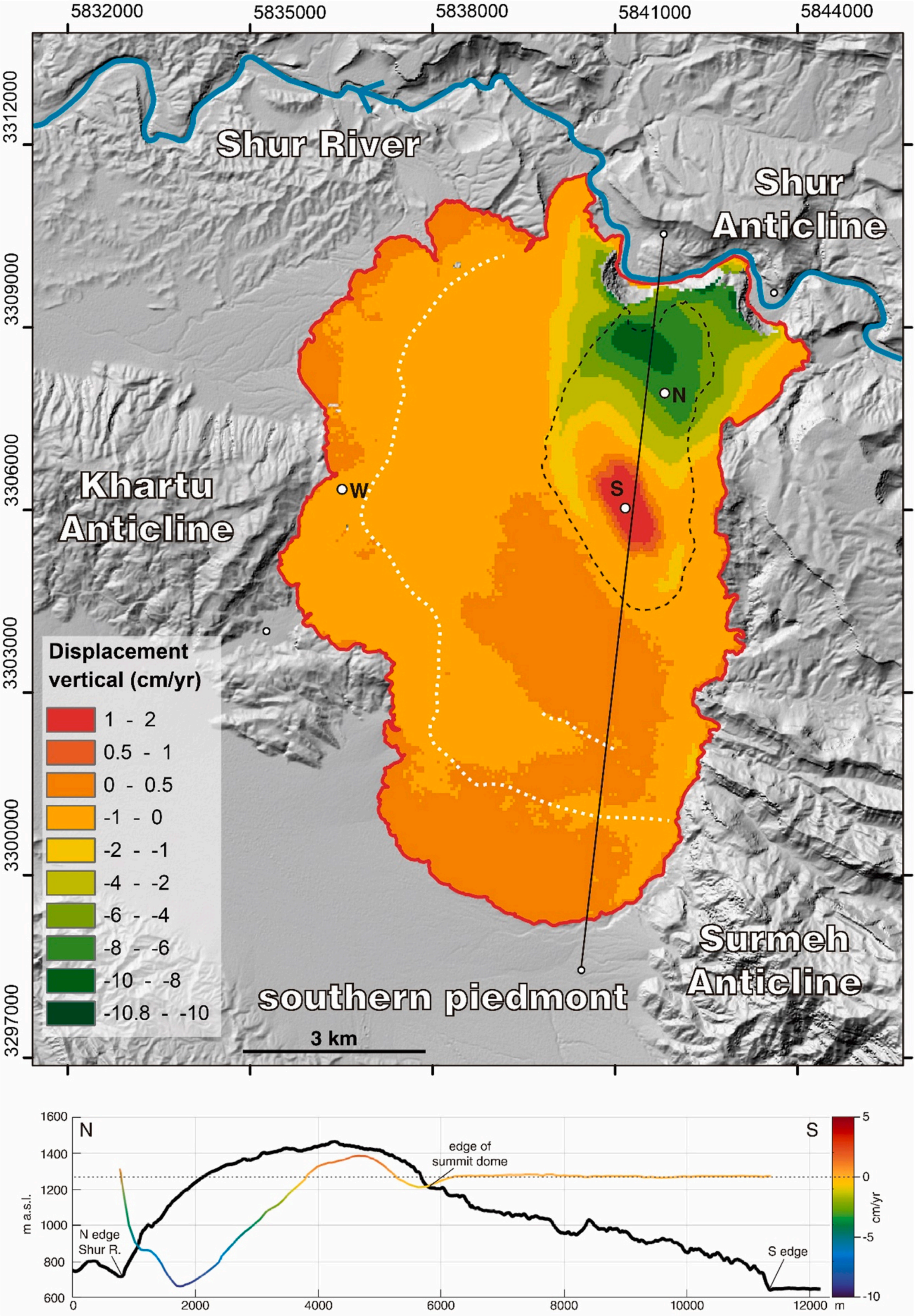

Fig. 11. Vertical displacement rate model of Jahani salt extrusion and N-S-oriented topographic and vertical deformation rate profiles covering the summit dome, the southern namakier, and the northern namakier trimmed and debuttressed by fluvial erosion. White dotted lines indicate distribution of ridges associated with non-evaporitic units. Displacement time series at points N, S and W shown in Fig. 13.

volume of 31 Hm^3 (calculated with a TIN derived for the DEM and the polygon volume tool). In the case of the 850 m scenario, the maximum values of lake depth, area, length and volume are 115 m, 6.6 km^2, 14.6 km and 211 Hm^3, respectively. The deeply entrenched and meandering morphology of the valley determined the development of a narrow and relatively sinuous lake.

4.5. *Kinematics of the salt fountain based on DInSAR data*

The current kinematics of the Jahani salt fountain can be

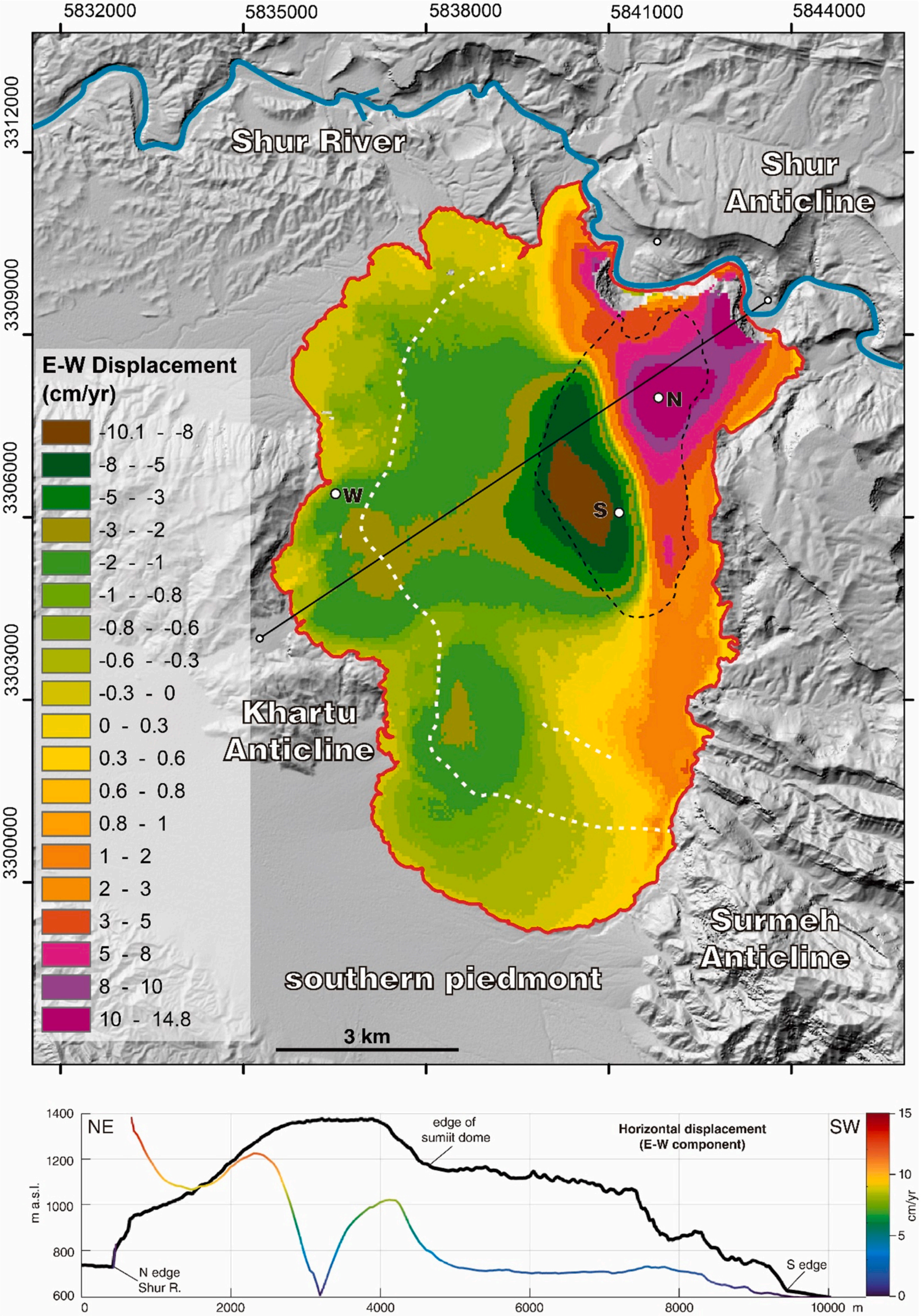

Fig. 12. Horizontal (E-W) displacement rate model of Jahani salt extrusion and NE-SW-oriented topographic and horizontal deformation rate profiles covering the summit dome and two namakiers, one laterally unconfined by fluvial erosion and another one unaffected by erosion at its front. Deformation rates in the profile are plotted as integer values (i.e., minus sign removed from westward displacement values). White dotted lines indicate distribution of ridges associated with non-evaporitic units. Displacement time series at points N, S and W shown in Fig. 13.

characterised with decomposed vertical and horizontal (E-W) displacement rate models derived from ascending and descending LOS data, together with deformation time series. Fig. 11 shows a spatially distributed model of vertical displacement rate for the salt extrusion. It also includes north-south topographic and displacement-rate profiles that illustrate the variations of vertical surface deformation across the summit dome and the main south- and north-flowing namakiers. These data reveal the significant role played by the loss of lateral confinement in the northern sector of the salt extrusion caused by the erosion of the Shur River, which has generated an extraordinary salt escarpment 6 km long and hundreds of meters in local relief (Gutiérrez et al., 2025) (Figs. 6F, 7A). The southern sector of the crestal zone of the summit dome, situated away from the erosional salt escarpment, is affected by an uplift rate of around 1–2 cm/yr. Conversely, the northern sector undergoes subsidence at rates that progressively increase towards the crest of the escarpment up to values of around −10 cm/yr. A band of high-subsidence occurs associated with the crest of the escarpment, where both salt flow and landsliding can operate in combination. The vertical displacement model indicates a progressive decrease in the subsidence rate within the salt escarpment towards the foot of the slope, although the data in this very steep terrain may have limited reliability due to SAR geometric distortions, such as shadow and layover, as well as errors in the DEM used for processing. In the northern namakier, the subsidence rate also decreases laterally to the east and west, away from the influence of the unloading effect of the escarpment (Fig. 11). In the southern portion of the summit dome and across its well-defined junction with the southern namakier, vertical displacement rates show the following spatial patterns: (1) decrease in the uplift rate towards the steep slope of the summit dome (from 2 to around 0 cm/yr; Fig. 6A); (2) apparent slow subsidence (0 to −1 cm/yr) around the summit dome-namakier junction where large internally drained depressions occur (Figs. 5, 6A); and (3) limited vertical displacement in the namakier (−1 to 0.5 cm/yr). The frontal sector of the NW and S lobes seem to be affected by some uplift (0–0.5 cm/yr), which is consistent with the lack

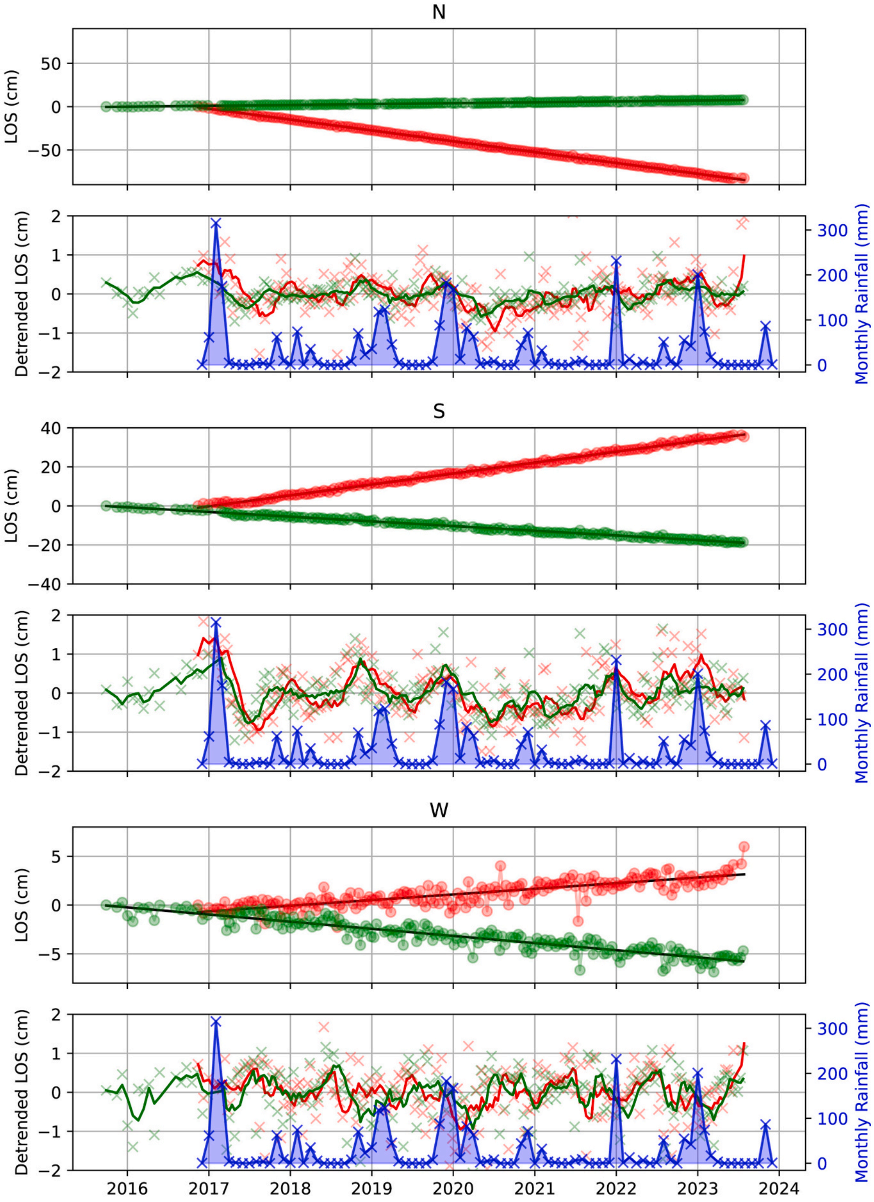

Fig. 13. Temporal variation of LOS displacement from ascending (red) and descending (green) data at three points of the salt fountain (locations indicated by N, S, and W in Figs. 11 and 12). For each point, the upper graph illustrates the LOS displacement time series and the lower graph monthly rainfall data from the Firuzabad station (20 km north of the study area) and residuals of the LOS displacement after removing the best-fit trend, plotted as discrete values and 2-month moving average.

of evidence of glacier retreat (e.g., moraine-like deposits), suggesting some advance and compressional flow (Fig. 6B, C).

Fig. 12 shows a horizontal (E-W) displacement rate model and coincident topographic and horizontal displacement rate profiles. A NE-SW trace has been selected for the profiles to cover the summit dome and the NE- and SW-directed salt glaciers. The displacement rate profiles indicate whole values (i.e., minus sign removed) for the E-W horizontal displacement component, which should be considered as minimum values for the actual horizontal displacement rate in the salt glaciers flowing to the NE and SW. Horizontal displacement in the salt fountain shows an asymmetric pattern: (1) horizontal displacement rates rise from null values in the axial zone of the dome crest to velocities around 8–10 cm/yr and 10–15 cm/yr in the SW and NE steep flanks of the summit dome, respectively; (2) displacement rates drop again towards the dome-namakier junction to 5–2 cm/yr and 8–10 cm/yr in the SW and NE, respectively; (3) in the SW namakier the horizontal velocity remains relatively constant at 1–2 cm/yr up to the frontal zone, where it drops to ~0 cm/yr; (4) in the NE namakier, the velocity rises abruptly up to 15 cm/yr at the laterally unconfined salt escarpment. Overall, the greater velocities in the NE sector of the salt fountain are in agreement with the presence of a large salt escarpment affected by fluvial erosion. Here, the salt glacier has a dominant N30E flow direction, thus actual horizontal flow rate should be around 1.15 times greater (cosec 30°) than the computed E-W components. The southern lobe also shows an asymmetric pattern with faster velocities along the oversteepened eastern flank, affected by fluvial undercutting that may induce some outward creep deformation.

In order to explore the temporal patterns of displacement and potential relationships with rainfall, we have constructed two types of graphs for a number of points of the salt fountain (Fig. 13): (1) LOS displacement time series from ascending (red) and descending (green) data; and (2) monthly rainfall data (2017–2024) from the Firuzabad meterological station (20 km to the N), alongside residuals of the LOS displacement data computed by removing the best-fit trend of the ascending (red) and descending (green) data, represented as discrete values and smoothed 2-month moving average. All displacements are referenced to a stable point at lat = 28.611° and lon = 52.502° (i.e., Garulizak limestone east of the salt fountain). The points shown in Fig. 13 include (see location in Figs. 11 and 12): (1) Point N located in the subsiding northen sector of the summit dome, where the E-displacement component peaks; (2) Point S situated in the rising southern sector of the summit dome, where positive vertical displacement peaks; and (3) Point W at the frontal sector of the W-directed lobe of the namakier. The linear trends of the LOS time series reveal continuous creep displacement at rather constant rates.

Because of differences in viewing geometries, cumulative LOS displacement vary between ascending and descending tracks and depending on whether the points are located in the summit dome (points N and S) or in a salt glacier (point W). For example, at point N, both subsidence and eastward motion project away from the sensor in ascending geometry, yielding approximately 90 cm of cumulative displacement over 6.5 year. In contrast, only ~10 cm of cumulative LOS displacement is observed over 8 years in descending geometry, where eastward motion and subsidence partially cancel the LOS displacement. Similarly, point S shows up to 40 cm and 20 cm of cumulative LOS displacement in ascending and descending geometries, respectively. In contrast, point W shows similar magnitudes of LOS displacement in both tracks, but in opposite directions, indicating predominantly horizontal movement.

To explore the potential relationships between temporal patterns of displacement and rainfall, we plotted the residuals of LOS deformation time series after removing the best-fit linear trend and compared them with monthly rainfall data from the Firuzabad meterorological station. The residuals exhibit short-term acceleration-deceleration episodes. These are partly related to measurement noise and atmospheric phase delays, which vary randomly over time. The residuals from the ascending and descending data are largely in phase (correlation coefficients of 0.6, 0.8, and 0.4 for points N, S, and W, respectively), suggesting that they are predominantly controlled by either vertical or north displacement components. At points N and W the residuals do not show high correlation with rainfall (correlation <±0.2 between rainfall and ascending or descending residuals), while at point S the residuals tend to coincide with rainfall (correlation coefficient of 0.4). Although the rainfall station is 20 km from the study area, it reflects the broader regional precipitation trends (i.e., more humid winters and drier summers), which largely coincide with the seasonal deformation pattern observed at point S.

5. Discussion

The orogen-oblique convergence between the Arabian and Eurasian plates has driven a deformation wave in the Simply Folded Belt of the Zagros that has propagated towards the foreland over the late Cenozoic. In the western Fars Arc, the style of the ongoing collisional deformation has been strongly influenced by the three-dimensional distribution of the Homuz salt detachment and associated diapirs, which function as strain localizers and enhancers. The main controlling factors include (Jahani et al., 2009, 2017; Hassanpour et al., 2018; Gutiérrez et al., 2024): (1) a 12–15 km thick supra-salt cover locally penetrated by pre-shortening diapirs; (2) thicker Hormuz salt on the hanging wall of down-to-the-E basement faults that controlled the Hormuz graben basins; and (3) rows of precursor salt structures overlain by thin and weak overburden associated with the aforementioned N- to NNW-oriented basement faults. The propagating surface deformation has been mainly accommodated through the development of buckle folds detached along the Hormuz salt, and oblique N- to NNW-trending dextral strike-slip faults that offset the folds (i.e., strain partitioning). These strike-slip faults likely correspond to supra-salt tear faults controlled by two linked factors (Jahani et al., 2017; Hassanpour et al., 2018): (1) more rapid translation of the cover above the thicker Hormuz salt located on the downthrown side of the E-dipping basement faults (i.e., lower basal friction); and (2) N- to NNW-oriented weak zones above the basement faults related to rows of precursor diapirs and thinned overburden. In the case of the Kareh Bas Fault, this concept is supported by the focal depth of the strike-slip earthquakes, mostly located above the deep salt detachment (Fig. 2B).

The inception of folding in the area around the Jahani salt extrusion occurred in Miocene times, as indicates the presence of basal onlaps and growth strata in the Gachsaran Formation on the northern limbs of the Aghar and Surmeh anticlines (Fig. 2; Hessami et al., 2001a). However, the onset of significant morphogenetic folding and relief creation under terrestrial conditions is recorded by the basal unconformity of the Bakhtyari conglomerates, that represents alluvial sedimentation sourced from growing anticlinal ridges. This major time-transgressive angular unconformity was situated by magnetochronological studies at 3.8 Ma on a fold situated in the same trend as the Jahani Diapir within the Fars Arc (Kuh-e-Ghol Anticline labelled in Fig. 1C; Ruh et al., 2014). The onset of strike-slip faulting in the study area probably postdates the initiation of significant folding (e.g., Authemayou et al., 2006). Assuming that the horizontal slip rate of 3.1–3.7 mm/yr obtained for the Kareh Bas Fault by GPS measurements has been constant (Tavakoli et al., 2008), and considering the cumulative offset of 4.5–5.5 km measured in the anticlines (Aghar, Khartu-Surmeh; Fig. 2), the onset of strike-slip faulting in the study area would have taken place at around 1.8–1.2 Ma, which is consistent with the suggested deformation sequence.

Cartographic evidence shows that the Kareh Bas S fault segment (Gutiérrez et al., 2024) comprises two fault strands with a right-stepping arrangement that overlap between the Konarsiah and the Jahani salt extrusions (Figs. 2 and 3). Data on strike-slip faults worldwide (Mann, 2007) and analogue experiments of strike-slip fault development (Holohan et al., 2008; Dooley and Schreurs, 2012 and references therein) reveal that weak zones such as diapirs promote the development of stepovers and fault segmentation. The eastern (and northern) strand of the Kareh Bas Fault likely propagated southwards and stepped over a precursor buried Jahani Diapir (or Konarsiah Diapir), initiating the development of the western (and southern) strand. The extension of the thin overburden above the precursor Jahani Diapir, now located at a releasing stepover, eventually created the opening through which the salt has emerged. The expelled salt initially generated a growing dome that has evolved into the present-day salt fountain. A similar strike-slip fault and diapir interaction-evolution has been proposed for the Dandenjan Diapir and the associated pull-apart basin to the north (Gutiérrez et al., 2024) (Fig. 2). The southward propagation of the Kareh Bas Fault across NW-SE-trending folds and the N-to-S sequential emergence of salt diapirs along this structure is supported by the morphological gradation of the salt extrusions, from mature degraded domes dominated by fluvial incision in the north, to the Jahani salt fountain with a well-defined summit dome (Gutiérrez et al., 2024). The 5 km long and 2.5 km wide summit dome of the Jahani salt fountain represents the surface expression of the vent feeding the extrusion, which probably has increased its size as transtensional deformation has progressed (Talbot and Alavi, 1996), potentially accompanied by a reduction in the velocity of salt rise (Fig. 5). The main driving force for the rise of the salt is most probably the contraction of the adjacent growing anticlines (i.e., contractional loading or squeezing), partially buried by the spreading namakiers, such as Khartu Anticline that shows a collapsed crest (Fig. 3).

Conclusive evidence of Quaternary deformation has been observed in the western strand of the Kareh Bas Fault, which has recurrently offset the older deposits of a +40 m terrace of the Shur River, while the uppermost sediments of the terrace remain undeformed (Fig. 4). The observed geometrical relationships together with the obtained OSL ages reveal a minimum of two surface faulting-folding events occurred before 14.7–13.8 ka and around 14.7–13.8 ka (i.e., most recent event). The latter sagged the unconsolidated alluvium creating a transverse synformal trough that was filled by anomalous well-sorted sand facies. Similar paleoseismic evidence was reported in a trench excavated across the Kazerun Fault (8.5 km N of Kamarij Diapir; Bachmanov et al., 2004), which exposed folded Quaternary sediments interpreted as coseismic bending of unconsolidated deposits. The authors inferred a minimum of two paleoearthquakes younger than 9 ka, with vertical displacement per event of around 1.5 m.

The segmentation of the Kareh Bas S fault, likely controlled precursor diapirs, has implications for seismic hazard analysis. The fault can be incorporated in seismic source models considering two scenarios: (1) 56 km long rupture encompassing the two strands and producing earthquakes with an expected magnitude of M_w 7.1 (Wells and Coppersmith, 1994); and (2) independent ruptures on the 32 km long eastern fault and the 42 km long western fault, generating earthquakes of M_w 6.8 and 7.0, respectively. The latter scenario involves lower earthquake magnitude, but significantly higher probability of having large damaging earthquakes. The two options can be considered using logic trees and assigning probabilities on the basis of statistical data derived from historical strike-slip earthquakes. A regression produced by Biasi and Wesnousky (2016) based on 46 mapped strike-slip surface ruptures indicate that the probability of a rupture passing through a stepover 1.7 km wide like the one in this case is around 55–60 %.

The numerical age obtained for the sands filling the synformal trough within the deposit of the +40 m terrace of the Shur River indicates that the aggradation of the upper 2.4 m thick gravel package and the subsequent 40 m of fluvial entrenchment occurred over a time lapse of 14.7–13.8 kyr, yielding a high long-term incision rate of 2.7–2.9 mm/yr. Both the age and the incision rate are comparable with values obtained by cosmogenic (^{10}Be, ^{36}Cl) and radiocarbon dating of terraces of the Dalaki and Mand rivers associated with active anticlinal structures in the western Fars Arc (Oveisi et al., 2009). At the hanging wall anticline of the reverse Mountain Front Fault (Gisakan Anticline), terrace deposits of the Dalaki River perched 70 m and 55 m above the river have been dated at 31 ± 1.5 cal. ka (radiocarbon on gastropods) and <44 ± 23 ka (maximum ^{10}Be burial age), providing long-term incision rates of 2,3 mm/yr and >1,3 mm/yr, respectively. Terraces of the Dalaki River lying at +40 m and +20 m in the reach between the Mountain Front Fault and the Kareh Bas Fault yielded ages of 12.5 ± 2.5 ka (exposure ^{36}Cl age) and 3.1 ± 0.7 ka (exposure ^{36}Cl age), indicating incision rates of 3.2 mm/yr and 6.7 mm/yr, respectively. Terraces of the Mand River associated with the Halikan Anticline (30 km S of Jahani) lying at +59 m and +40 m were dated at 44 ± 10 ka (exposure ^{10}Be age) and 15.2 ± 3.8 ka (exposure ^{10}Be age) indicating long-term incision rates of 1.3 mm/yr and 2.6 mm/yr, respectively. The multiple local incision rates estimated by Oveisi et al. (2009) suggest the following spatial-temporal patterns: (1) general rapid incision in a collisional context of regional uplift; (2) faster incision in structural highs (anticlines, hanging walls of reverse faults), and specially in those close to the deformation front; and (3) higher incision rates after the formation of intermediate terraces (ca. +40–50 m). The high downcutting rate of 2.7–2.9 mm/yr estimated in this work for the Shur River suggest that the region around the Jahani salt extrusion, and specifically the Shur Anticline are experiencing rapid uplift. The presence of a marl-dominated bedrock (Mishan Formation) facilitate rapid adjustments in the longitudinal profile of the river. Additionally, periods of enhanced local incision may have also occurred following episodes of river damming in upstream valley sections (i.e., salt-glacier dams).

The Jahani salt fountain, covering 67.9 km^2, with a local relief of 918 m, and with a prominent summit dome 250 m high, is one of the largest and topographically more energetic salt extrusions in the Fars Arc of the Zagros Mountains (Talbot and Alavi, 1996; Talbot et al., 2000; Abirifard et al., 2017) (Figs. 5, 6, 7). A remarkable feature of this salt fountain is that its northern namakier interacts with a major river, which has carved a sinuous salt escarpment 6 km long and locally more than 400 m high (Figs. 5, 6F, 7A). Two antagonistic geomorphic trends operate in this exceptional setting. On the one hand, fluvial undermining induces rocksalt landslides leading to scarp retreat. On the other hand, rapid salt flow favoured by the erosional debuttressing of the namakier tends to deflect and block the Shur River. The distribution of large disconnected masses of Hormuz salt and residual Hormuz deposits reveals that that the northern namakier blocked the Shur River in the past at least once, creating a dam that surmounted the opposite valley margin as much as 120 m (Figs. 5, 7). The presence of lacustrine deposits in a tributary drainage upstream of the damming site corroborates the development of a namakier-dammed lake (Fig. 9). To our knowledge, this is the first work that documents the blockage of a major river by a salt glacier.

An OSL age estimate of 28 ± 5 ka has been obtained from the lake deposits. Two paleogeographic scenarios have been reconstructed considering the current topography and lakes with water levels at 800 m a.s.l. (top of lacustrine deposits) and 850 m a.s.l. (spill level of the remnants of the natural dam), resulting in narrow and sinuous lakes 6.3 and 14.6 km long and with maximum depths of 65 and 115 m, respectively (Fig. 10). However, the long-term incision rate estimated with the OSL ages from the +40 m terrace deposit of the Shur River (2.7–2.9 mm/yr) suggests that the river may have experienced as much as 75–80 m of incision since the deposition of the lake deposits at around 28 ka, pointing to a shallow lake by that time, developed when the base level was at a significantly higher elevation. A likely explanation is that the river has experienced multiple damming episodes, and that the analysed lacustrine deposits correspond to a damming phase older than the one recorded by the mapped bodies of disconnected Hormuz located on the northern bank of the river. This interpretation is supported by the following data: (1) the mapped Hormuz dam is inset with respect to the +40 m terrace, and consequently should be younger than 14.7–13.8 ka (Figs. 5, 6F, 7A); (2) the dated paleolake deposits are much more indurated than the +40 m terrace deposits, supporting the older OSL age (28 ± 5 ka) derived from them. Consequently, based on the available cartographic and geochronological data, we interpret at least two damming episodes, one occurred around 28 ka and a more recent one with conspicuous geomorphic imprint younger than 14.7–13.8 ka. It is likely that the damming episodes occurred during relatively dry and low-discharge periods, when the erosional capacity of the Shur River was overwhelmed by the progressive advance of the namakier. Landsliding can be ruled out as a potential damming mechanism, based on the characteristics, extent and distribution of the Hormuz sediments mapped on the northern margin of the valley (Fig. 5). The ca. 28 ka event took place during the Last Glacial Maximum (MIS 2), characterised by dry and cold conditions in Iran (Kehl, 2009; Rostami et al., 2024 and references therein). Probably, during the damming phases, undersaturated water could flow through the porous gravelly alluvium beneath the salt glacier, eventually creating subglacial tunnels. The section of these caves can grow rapidly by forced currents flowing against highly soluble salt and eventually collapse evolving into incised valleys with throughgoing surface flow.

Overall, the computed DInSAR data including decomposed vertical and horizontal (E-W) displacement reveal that Jahani is currently a growing and most probably an expanding salt fountain (Figs. 11, 12). Nonetheless, its kinematics in the NE sector is strongly altered and accelerated by the presence of the large escarpment carved by the Shur River, where the salt has been debuttressed. The crest of the summit dome experiences uplift at rates of around 1–2 cm/yr on its southern sector, away from the influence of the erosional escarpment. Conversely, the northern sector, flowing towards the Shur Valley, is affected by rapid subsidence at rates that increase up to around −10 cm/yr towards the crest of the escarpment. Horizontal displacement also shows higher values in the portion of the summit dome associated with the escarpment (10–15 cm/yr) than on the opposite side unaffected by erosional unloading (8–10 cm/yr). In the salt outcrops of the escarpment, the observed downward displacement can be related to the contribution of both salt flow and salt dissolution, the latter with an annual rate of vertical denudation roughly estimated at around 8–12 cm/yr by Bruthans et al. (2008). The namakiers are spreading away from the summit dome towards the surrounding topographic lows at rates of around 1–2 cm/yr. With the exception of the "salt cascade" in the NE sector, the displacement rates decrease towards the glacier fronts as the perimeter of the salt fountain increases and the flow lines diverge. The glacier fronts seem to experience limited advance and some uplift ascribable to compressional flow. Greater horizontal velocities are observed around steep salt slopes, such as the flanks of the summit dome or the eastern side of the southern namakier, affected by fluvial undercutting.

Barnhart and Lohman (2012), in a regional InSAR study of salt extrusions in the Fars Arc (Envisat C-band data, 2003–2010; detection threshold ca. 3 mm/yr), classified as continuously active the three diapirs associated with the southern segments of the Kareh Bas fault zone (Konarsiah, Jahani and Bahar), but not the remaining ones to the north (Dandenjan, Meygor and Salamati; Fig. 2). Talbot et al. (2000), within the framework of a project aimed at understanding the kinematics of salt structures for practical purposes (e.g., geostorage, hydrocarbon reservoirs sealed by salt sheets), carried out geodetic surveys at Jahani salt extrusion. They measured vertical displacement and apparent horizontal displacement in 43 markers measured from three theodolite stations over three 12–18-months-long time intervals spanning a total of 4.5 years. The obtained displacement values and rates, mostly of the order of meters per year, exhibited a highly erratic spatial and temporal pattern difficult to conciliate with the geomorphology of the salt fountain. Regarding the vertical displacements, a number of markers indicated inconsistent uplift and subsidence in consecutive years, often with extremely high values. For instance, the same marker in the crestal zone of the summit dome showed no vertical displacement in one interval and a subsidence rate of 12 m/yr in the following one. Similarly, the measurements of one interval indicated that a significant proportion of the southern namakier is dominated by decimeter- to meter-scale uplift, while in the subsequent one subsidence of a similar magnitude prevailed. The apparent horizontal displacement values also showed difficult-to-justify haphazard patterns, including portions of salt glaciers apparently flowing upslope, and substantial variations in magnitude and sense of displacement in successive intervals. For instance, the apparent horizontal displacement of one marker in the northern namakier varied from 24.5 m in the first interval to values close zero in the following ones. Based on the obtained measurements, they carried a numerical simulation to reconstruct the evolution of the salt fountain considering a vertical salt extrusion rate of 2–3 m/yr through an orifice 1.7 km in diameter (ca. 5 10^6 m^3/yr) and assuming a constant dissolution rate of 2–3 cm/yr. According to their simulation, the extrusion of salt started at around 55 ka and the total volume of salt expelled at Jahani amounts 200 km^3. Note that this value is two orders of magnitude higher that the current volume (ca. 8.5 km^3) and that would involve an average salt thickness of around 3 km. Talbot et al. (2000) indicated that the high volume of salt expelled suggests that the ca. 1 km thick Hormuz salt source should be close to exhaustion or isolation (primary welding). The enormous deviation between the displacement values reported in Talbot et al. (2000), and the geomorphologically consistent DInSAR measurements reported in this work, as well as in other publication dealing with salt extrusions in the Zagros (Aftabi et al., 2010; Ghassemi and Roustaei, 2021; Shami et al., 2024) or in central Iran (Abdolmaleki et al., 2014; Roosta et al., 2019; Mohammadnia et al., 2021), and worldwide (Pérez-Villar et al., 2025), strongly suggests that the former lack validity. In agreement with the discussion presented by Bruthans et al. (2024), the large discrepancy, can be attributed to the inadequate methodology applied by Talbot et al. (2000), including the use of improper markers (bushes, blocks, cairns, salt pillars), the installation of one theodolite station on the NW namakier (i.e., mobile site), and the fact that none of the markers could not be identified from more than one theodolite station, precluding estimating actual horizontal displacement and assessing the internal consistency. The proposed lack of validity of the data published by Talbot et al. (2000) also invalidates the extremely young age estimated for the Jahani salt fountain, which is not in agreement with the geological history of the region (i.e., timing of folding and strike-slip faulting; Jackson and Hudec, 2017; Gutiérrez et al., 2024).

The LOS displacement time series show continuous displacement at a rather constant rate. The small temporal variations of the displacement show some correlation with rainfall data in the crest of the summit dome (point S). However, it is not clear the underlying processes responsible for this small and local temporal variability (swelling of capsoil?, accelerated salt rise?). Further studies using InSAR and precipitation data with higher spatial and temporal resolution could shed light into this issue. The data from Jahani do not align with the poorly substantiated concept whereby salt extrusions in the Zagros are characterised by long periods of near-stasis punctuated by short intervals of rapid displacement following rainfall events (Talbot and Pohjola, 2009 and references therein). According to this model of episodic kinematics, destressing and dissolution in the outer zone of the salt extrusion produces a fractured carapace a few meters thick that functions as a restraining corset during dry periods. Presumably rainfall events weaken this stiff and permeable outer shell by dissolution promoting surges. However, it seems unlikely that a thin and densely fractured outer carapace has sufficient strength to restrain the gravitational spreading in salt extrusions hundreds of meters thick. Additional ground displacement and precipitation data from salt extrusions of different morphological types are needed to better understand the temporal patterns of salt flow.

An important consideration for our analysis is the limitations related to the two-track decomposition into vertical and east-west components. The geometry of the two tracks shows that LOS measurements are highly sensitive to vertical displacement (sensitivity≈ -0.8) and eastward movement (sensitivity≈ -0.6 for ascending and ≈ 0.6 for descending). In contrast, LOS sensitivity to northward movement is only about -0.1. For example, a pure subsidence of 10 cm projects into 8 cm of LOS deformation, while 10 cm of eastward movement appears as 6 cm of LOS deformation away from the sensor in ascending track and towards the sensor in descending track. Conversely, 10 cm of northward movement leads to only 1 cm of LOS deformation. Considering that LOS measurements are more sensitive to vertical and east-west movements, and that we only have two LOS observations for three unknown deformation components, we have chosen to disregard the north component. This may introduce bias in regions where northward movement is substantial such as in the northern sector of the summit dome (e.g., point N). Since the signs of vertical and north sensitivities are the same in our datasets, ignoring the north component may bias the estimation of vertical deformation, such that a 10 cm northward displacement could bias the up component by 1.25 cm. This bias should not have a significant impact in most areas and does not affect the core of our interpretations. Nevertheless, in areas where the north component is substantial, such as the northern sector of the salt extrusion flowing towards the Shur valley, estimation of vertical component might be under or over-estimated.

6. Conclusions

The analysis of the Jahani salt extrusion and the associated right-lateral Kareh Bas Fault, based on the integration of field, cartographic, geochronological and DInSAR data, has resulted in the following main findings:

A precursor and buried Jahani Diapir (and or Konarsiah Diapir) likely controlled the westward stepping of the S-propagating Kareh Bas Fault, resulting in two fault strands separated by an overlapping right-releasing stepover. The pulling apart of the thin cover above the diapir at this transtensional zone eventually promoted the emergence of the salt diapir, rejuvenated by contractional loading operating in the nearby anticlines. Jahani is the youngest salt extrusion of the row of emergent diapirs associated the Kareh Bas N-S fault segments. The Kareh Bas Fault, as supports the focal depth of strike-slip faults in the area, is most probably a supra-salt tear fault, but with sufficient potential rupture area to generate Mw ~ 7 earthquakes, given the high depth of the salt detachment (12–15 km).

The deposits of the +40 m terrace of the Shur River record two paleoarthquakes on the western strand of the Kareh Bas Fault, occurred before and around 14.7–13.8 ka. The OSL ages obtained from the terrace deposits indicate a long-term incision rate of 2.7–2.9 mm/yr for the Shur River, consistent with estimates reported in previous publications. The high downcutting rate points to high uplift rates, potentially enhanced during some periods by upstream damming episodes.

The distribution of disconnected masses of Hormuz salt and residual Hormuz deposits, together with paleolake sediments, reveal that the northern glacier of the Jahani salt fountain has recurrently blocked the Shur River and created namakier-dammed lakes upstream. OSL ages and cartographic relationships indicate that a damming episode occurred at around 28 ka and at least another one after 14.7–13.8 kyr.

Overall, the Jahani salt fountain can be considered as a growing and expanding salt fountain. The southern portion of the summit dome rises vertically and expands laterally at rates as high as 1–2 cm/yr and 8–10 cm/yr, respectively. Conversely, the southern portion, affected by the debuttressing effect of the large salt escarpment carved by the Shur River experiences rapid downward flow with vertical and horizontal rates that reach around −10 cm/yr and 10–15 cm/yr. The surrounding salt glaciers are flowing outwards at horizontal rates of around 2 cm/yr that decrease distally as the perimeter of the salt fountain increases. The computed DInSAR data reveal that the previously published rates based on poor theodolite measurements overestimated the kinematics of the salt fountain by two orders of magnitude and led to an inconsistent age estimate for the salt extrusion.

The LOS displacement time series show continuous salt flow at rather constant rates. This temporal pattern does not align with the previously proposed model of episodic kinematics whereby long periods of quiescence are interrupted by surging events triggered by rainfall. Additional DInSAR studies covering salt extrusions at different evolutionary stages and in variable tectonic (associated and non-associated with faults), geomorphic (confined versus unconfined) and climatic settings will contribute to better constrain their kinematics and controlling factors.

CRediT authorship contribution statement

Francisco Gutiérrez: Writing – original draft, Resources, Project administration, Methodology, Investigation, Funding acquisition, Formal analysis, Data curation, Conceptualization. **Mahmud Haghshenas Haghighi:** Writing – original draft, Software, Formal analysis, Data curation. **Issa Ilyati:** Writing – review & editing, Investigation, Data curation. **Mahdi Motagh:** Writing – review & editing, Conceptualization. **Miren del Val:** Writing – review & editing, Software, Data curation.

Declaration of competing interest

The authors declare the following financial interests/personal relationships which may be considered as potential competing interests: Francisco Gutierrez reports financial support was provided by University of Zaragoza. Francisco Gutierrez reports a relationship with University of Zaragoza that includes:. If there are other authors, they declare that they have no known competing financial interests or personal relationships that could have appeared to influence the work reported in this paper.

Acknowledgements

The authors are very grateful to Prof. Mohsen Rezaei and Prof. Mehdi Zarei for logistical assistance and to Dr. Vince Matthews for reviewing a draft of the mansucript. Edwin Nissen and Ezgi Karasözen kindly provided data from their relocated earthquake catalog of the Fars Arc. We are also very grateful to two anonymous reviewers for their insightful comments. The work has been supported by the Salvador de Madariaga grant (PRX22/00029) and project DIAPERNO (PID 2021-123189NB-I00) of the Spanish Government (Ministerio de Ciencia e Innovación). The TanDEM-X digital elevation models were provided by the German Aerospace Center (grant DEMGEOL288).

Appendix A. Supplementary data

Supplementary data to this article can be found online at https://doi.org/10.1016/j.geomorph.2025.109955.

Data availability

Data will be made available on request.

References

Abdolmaleki, N., Motagh, M., Bahroudi, A., Sharifi, M.A., Haghshenas Haghighi, M., 2014. Using Envisat InSAR time-series to investigate the surface kinematics of an active salt extrusion near Qum, Iran. Journal of Geodynamics 81, 56–66. https://doi.org/10.1016/j.jog.2014.07.001.

Abirifard, M., Raeisi, E., Zarei, M., Zare, M., Filippi, M., Bruthans, J., Talbot, C.J., 2017. Jahani Salt Diapir, Iran: hydrogeology, karst features and effect on surrounding environment. Int. J. Speleol. 46, 445–457.

Aftabi, P., Roustaie, M., Alsop, G.I., Talbot, C.J., 2010. InSAR mapping and modelling of an active Iranian salt extrusion. J. Geol. Soc. London 167 (1), 155–170. https://doi.org/10.1144/0016-76492008-165.

Aitken, M.J., Xie, J., 1990. Moisture correction for annual gamma dose. Anc. TL. 8, 6–9.

Ambraseys, N.N., Jackson, J.A., 1998. Faulting associated with historical and recent earthquakes in the eastern Mediterranean region. Geophys. J. Int. 133, 390–406.

Ambraseys, N.N., Melville, C.P., 1982. A History of Iranian Earthquakes. Cambridge University Press, Cambridge.

Authemayou, C., Chardon, D., Bellier, O., Malekzadeh, Z., Shabanien, E., Abbassi, M., 2006. Late Cenozoic partitioning of the oblique plate convergence in the Zagros fold-and-thrust belt (Iran). Tectonics 25, TC3002.

Authemayou, C., Bellier, O., Chardon, D., Benedetti, L., Malekzade, Z., Claude, C., Angeletti, B., Shabanian, E., Abbassi, M.R., 2009. Quaternary slip-rates of the Kazerun and the Main Recent Faults: active strike-slip partitioning in the Zagros fold-and-thrust belt. Geophys. J. Int. 178, 524–540.

Bachmanov, D.M., Trifonov, V.G., Hessami, K.T., Kozhurin, A.I., Ivanova, T.P., Rogozhin, E.A., Hademi, M.C., Jamali, F.H., 2004. Active faults in the Zagros and Central Iran. Tectonophysics 380, 221–241.

Barnhart, W.D., Lohman, R.B., 2012. Regional trends in active diapirism revealed by mountain range-scale InSAR time series. Geophys. Res. Lett. 39 (8), L08309.

Berardino, P., Fornaro, G., Lanari, R., Sansosti, E., 2002. A new algorithm for surface deformation monitoring based on small baseline differential SAR interferograms. IEEE Trans. Geosci. Remote Sens. 40 (11), 2375–2383.

Berberian, M., 1995. Master "blind" thrust faults hidden under the Zagros folds: active basement tectonics and surface morphotectonics. Tectonophysics 241, 193–224.

Berberian, M., 2014. Earthquakes and Coseismic Surface Faulting on the Iranian Plateau. Elsevier, Amsterdam.

Berberian, M., Tchalenko, J.S., 1976. Earthquakes of southern Zagros (Iran): Bushehr region. Geological Survey of Iran 39, 343–369.

Biasi, G.P., Wesnousky, S.G., 2016. Steps and gaps in ground ruptures: empirical bounds on rupture propagation. Bull. Seismol. Soc. Am. 106, 1110–1124.

Brennan, B.J., 2003. Beta doses to spherical grains. Radiat. Meas. 37, 299–303.

Brennan, B.J., Lyons, R.G., Phillips, S.W., 1991. Attenuation of alpha particle track dose for spherical grains. Int. J. Radiat. Appl. Instrum. Nucl. Tracks Radiat. Meas. 18, 249–253.

Bruthans, J., Asadi, N., Filippi, M., Vilhelm, Z., Zare, M., 2008. A study of erosion rates on salt diapir surfaces in the Zagros Mountains, SE Iran. Environ. Geol. 53, 1079–1089.

Bruthans, J., Filippi, M., Asadi, N., Zare, M., Slechta, S., Churackova, Z., 2009. Surficial deposits on salt diapirs (Zagros Mountains and Persian Gulf Platform, Iran): characterization, evolution, erosion and the influence on landscape morphology. Geomorphology 107, 195–209.

Bruthans, J., Kamas, J., Filippi, M., Zare, M., Mayo, A.L., 2017. Hydrogeology of salt karst under different cap soils and climates (Persian Gulf and Zagros Mts., Iran). International Journal of Speleology 46, 303–320.

Bruthans, J., Filippi, M., Slavík, M., Závada, P., Zare, M., 2024. Rapid evolution of salt glacier caves on a mountain diapir in a semiarid climate. Geomorphology 448, 109058.

Callot, J.P., Jahani, S., Letouzey, J., 2007. The role of pre-existing diapirs in fold and thrust belt development. In: Lacombe, O., Roure, F., Lavé, J., Vergés, J. (Eds.), Thrust Belts and Foreland Basins. Springer, Berlin, pp. 1–17.

De Waele, J., Gutiérrez, F., 2022. Karst Hydrogeology, Geomorphology and Caves. Wiley, Chichester.

Dewey, J.W., Grantz, A., 1973. The Ghir earthquake of April 10, 1972 in the Zagros Mountains of southern Iran: seismotectonic aspects and some results of a field reconnaissance. Bull. Seismol. Soc. Am. 63, 2071–2090.

Dooley, T.P., Schreurs, G., 2012. Analogue modelling of intraplate strike-slip tectonics: a review and new experimental results. Tectonophysics 574-575, 1–71.

Duller, G.A.T., 2008. Luminescence Dating. English Herit.

Durcan, J., King, G., Duller, G.A.T., 2015. DRAC: Dose Rate and Age Calculator for trapped charge dating. Quat. Geochronol. 28, 54–61.

Faghih, A., Nezamzadeh, I., Kusky, T., 2016. Geomorphometric evidence of an active pop-up structure along the sabzpushan fault zone, Zagros mountains, SW Iran. J. Earth Sci. 27, 945–954.

Fakhari, M.D., Axen, G.J., Horton, B.K., Hassanzadeh, J., Amini, A., 2008. Revised age of proximal deposits in the Zagros foreland basin and implications for Cenozoic evolution of the High Zagros. Tectonophysics 451, 170–185.

Fattahi, H., Amelung, F., 2013. DEM error correction in InSAR time series. IEEE Trans. Geosci. Remote Sens. 51 (7), 4249–4259.

Galbraith, R.F., Roberts, R.G., Laslett, G.M., Yoshida, H., Olley, J.M., 1999. Optical dating of single and multiple grains of quartz from Jinmium rock shelter, Northern Australia: part 1, experimental design and statistical models. Archaeometry 41, 339–364.

Ghassemi, M.R., Roustaei, M., 2021. Salt extrusion kinematics: insights from existing data, morphology and InSAR modelling of the active emergent Anguru diapir in the Zagros fold and thrust belt, Iran. Journal of the Geological Society 178 (6), jgs2020-136. https://doi.org/10.1144/jgs2020-136.

Goldstein, R.M., Werner, C.L., 1998. Radar interferogram filtering for geophysical applications. Geophys. Res. Lett. 25 (21), 4035–4038.

GSI, 1996. Geological Map of Iran 1:100.000 series. Darenjan sheet. Geological Survey of Iran, Tehran.

GSI, 2009. Geological Map of Iran 1:100.000 series. Firoozabad sheet. Geological Survey of Iran, Tehran.

Guérin, G., Mercier, N., Adamiec, G., 2011. Dose-rate conversion factors: update. Ancient TL 29, 5–8.

Guérin, G., Mercier, N., Nathan, R., Adamiec, G., Lefrais, Y., 2012. On the use of the infinite matrix assumption and associated concepts: a critical review. Radiat. Meas. 47, 778–785.

Gutiérrez, F., Deirnik, H., Zarei, M., Medialdea, A., 2023a. Geology, geomorphology and geochronology of the coseismic? Emad Deh rock avalanche associated with a growing anticline and a rising salt diapir, Zagros Mountains, Iran. Geomorphology 421, 108527.

Gutiérrez, F., Zarei, M., Hudec, M.R., Deirnik, H., 2023b. Normal faulting and landsliding in morpho-structural domes related to buried salt stocks, Zagros Mountains, Iran. insights into salt breakout. Mar. Pet. Geol. 155, 106376.

Gutiérrez, F., Ilyati, I., Rezaei, M., Zarei, M., Hudec, M., 2024. Active strike-slip faulting, diapirism and seismic hazards. The case of the Kareh Bas fault and the associated Dandenjan salt extrusion in the zagros Mountains, SW Iran. J. Struct. Geol. 187, 105239.

Gutiérrez, F., Ilyati, I., Zarei, M., 2025. Surface karst geomorphology in the Jahani salt extrusion, Zagros Mountains, Iran. Geomorphology, 109859.

Harrison, J.V., 1930. The geology of some salt-plugs in Laristan, southern Persia. Quarterly Journal of the Geological Society 86, 463–522.

Harvey, A., 2007. High-sinuosity bedrock channels: response to rapid incision. Examples in NE Spain. Cuaternario y Geomorfología 21, 21–47.

Hassanpour, J., Jahani, S., Ghassemi, M.R., Alavi, S.A., Zeinali, F., 2018. Evolution of the Karebas Fault System and adjancent folds, central Zagros fold-and-thrust belt, Iran: role of pre-existing halokinesis (salt structures and minibasins) and detachment levels. J. Asian Earth Sci. 164, 125–142.

Hessami, K., Koyi, H.A., Talbot, C.J., Tabasi, H., Shabanian, E., 2001a. Progressive unconformities within an evolving foreland fold–thrust belt, Zagros Mountains. J. Geol. Soc. London 158, 969–981.

Hessami, K., Koyi, H.A., Talbot, C.J., 2001b. The significance of strike-slip faulting in the basement of the Zagros fold and thrust belt. Journal of Petroleum Geology 24, 5–28.

Hogenson, K., Kristenson, H., Kennedy, J., Johnston, A., Rine, J., Logan, T., Zhu, J., Williams, F., Herrmann, J., Smale, J., Meyer, F., 2020. Hybrid Pluggable Processing Pipeline (HyP3): A Cloud-native Infrastructure for Generic Processing of SAR Data [Computer Software]. https://doi.org/10.5281/zenodo.4646138.

Holohan, E.P., van Wyk de Vries, B., Troll, V.R., 2008. Analogue models of caldera collapse in strike-slip tectonic regimes. Bull. Volcanol. 70, 773–796.

Homke, S., Vergés, J., Garcés, M., Emami, H., Karpuz, R., 2004. Magnetostratigraphy of Miocene-Pliocene Zagros foreland deposits in the front of the Push-e Kush arc (Lurestan Province, Iran). Earth Planet. Sci. Lett. 225, 397–410.

Jackson, M.P.A., Hudec, M.R., 2017. Salt Tectonics. Principles and Practice. Cambridge University Press, Cambridge.

Jahani, S., Callot, J.P., Frizon de Lamotte, D., Letouzey, J., Leturmy, P., 2007. The salt diapirs of the eastern Fars Province (Zagros, Iran): a brief outline of their past and present. In: Lacombe, O., Roure, F., Lavé, J., Vegés, J. (Eds.), Thrust Belts and Foreland Basins. Springer, Berlin, pp. 289–308.

Jahani, S., Callot, J.P., Letouzey, J., Frizon de Lamotte, D., 2009. The eastern termination of the Zagros Fold-and-Thrust Belt, Iran: structures, evolution, and relationships between salt plugs, folding, and faulting. Tectonics 28, TC6004.

Jahani, S., Hassanpour, J., Mohammadi-Firouz, S., Letouzey, J., de Lamotte, D.F., Alavi, S.A., Soleimany, B., 2017. Salt tectonics and tear faulting in the central part of the Zagros Fold-Thrust Belt, Iran. Marine and Petroleum Geology 86, 426–446.

Karasözen, E., Nissen, E., Bergman, E.A., Ghods, A., 2019. Seismotectonics of the Zagros (Iran) from orogen-wide, calibrated earthquake relocations. J. Geophys. Res. Solid Earth 124, 9109–9129.

Kehl, M., 2009. Quaternary climate change in Iran. The state of knowledge. Erdkunde 63, 1–17.

Kent, P.E., 1958. Recent studies of south Persian salt plugs. AAPG Bull. 42 (12), 2951–2972.

Kent, P.E., 1979. The emergent Hormuz salt plugs of southern Iran. J. Pet. Geol. 2, 117–144.

Khadivi, S., Mouthereau, F., Larrasoaña, J.C., Vergés, J., Lacombe, O., Khademi, E., Beamud, E., Melinte-Dobrinescu, M., Suc, J.P., 2010. Magnetochronology of synorogenic Miocene foreland sediments in the Fars Arc of the Zagros Folded Belt (SW Iran). Basin Res. 22, 918–932.

Letouzey, J., Sherkati, S., 2004. Salt Movement, Tectonic Events, and Structural Style in the Central Zagros Fold and Thrust Belt (Iran). In: 24th Annual GCSSEPM Foundation. Bob F. Perkins Research Conference: Salt-Sediment Interactions and Hydrocarbon Prospectivity: Concepts, Applications, and Case Studies for the 21st Century, Gulf Coast Section. Society for Sedimentary Geology, Houston, Texas.

Mann, P., 2007. Global catalogue, classification and tectonic origins of restraining and releasing bends on active and ancient strike-slip fault systems. In: Cunningham, W. D., Mann, P. (Eds.), Tectonics of Strike-Slip Restraining and Releasing Bends, 290. Geological Society, London, Special Publications, pp. 13–142.

Mohammadnia, M., Najafi, M., Mousavi, Z., 2021. InSAR constraints on the active deformation of salt diapirs in the Kalut basin, Central Iran. Tectonophysics 810, 228860. https://doi.org/10.1016/j.tecto.2021.228860.

Molinaro, M., Leturmy, P., Guezou, J.C., Frizon de Lamotte, D., Eshraghi, S.A., 2005. The structure and kinematics of the southeastern Zagros fold-thrust belt, Iran: from thin-skinned to thick-skinned tectonics. Tectonics 24, TC3007.

Moreno, D., Richard, M., Bahain, J., Duval, M., Falguères, C., Tissoux, H., Voinchet, P., 2017. ESR dating of sedimentary quartz grains: some basic guidelines to ensure optimal sampling conditions. Quaternaire 28, 161–166.

Moreno, D., Gutiérrez, F., del Val, M., Carbonel, D., Jiménez, F., Alonso, M.J., Martínez-Pillado, V., Guzmán, O., López, G.I., Martínez, D., 2021. A multi-method dating approach to reassess the geochronology of faulted Quaternary deposits in the central sector of the Iberian Chain (NE Spain). Quaternary Geochronology 65, 101185.

Motiei, H., 1993. Stratigraphy of Zagros. Geological Survey of Iran, Tehran.

Mouthereau, F., Tensi, J., Bellahsen, N., Lacombe, O., De Boisgrollier, T., Kargar, S., 2007. Tertiary sequence of deformation in a thin-skinned/thick-skinned collision belt: the Zagros Folded Belt (Fars, Iran). Tectonics 26, TC5006.

Murray, A.S., Wintle, A.G., 2000. Luminescence dating of quartz using an improved single-aliquot regenerative-dose protocol. Radiation Measurement 37, 377–381.

Murray, A.S., Wintle, A.G., 2003. The single aliquot regenerative dose protocol: potential for improvements in reliability. Radiat. Meas. 32, 57–73.

Nezamzadeh, I., Faghih, A., Oveisi, B., Kusky, T., Khajavi, N., Soleimani, M., Meng, J., 2024. On the use of displaced river terraces to characterize active tectonics of the Zagros orogenic belt, SW Iran. Results in Earth Sciences 2, 100045.

Oveisi, B., Lavé, J., van der Beek, P., Carcaillet, J., Benedetti, L., Aubourg, C., 2009. Thick- and thin-skinned deformation rates in the central Zagros simple folded zone (Iran) indicated by displacement of geomorphic surfaces. Geophys. J. Int. 176, 627–654.

Pepe, A., Lanari, R., 2006. On the extension of the minimum cost flow algorithm for phase unwrapping of multitemporal differential SAR interferograms. IEEE Trans. Geosci. Remote Sens. 44 (9), 2374–2383.

Pérez-Villar, G., Gutiérrez, F., Bausilio, G., Di Martire, D., 2025. Integrating DInSAR and detailed mapping for characterizing ground displacement in the Cardona salt extrusion related to diapiric uplift, disolutional lowering, landsliding and sinkholes. Eng. Geol. 352, 108068.

Perry, J.T.O'.B., Setudehnia, A., Nars, M., 1965. South-East Fars Geological Compilation Map at 1:250,000. Iranian Oil Operating Companies, Geological and Exploration Division, Tehran.

Prescott, J.R., Hutton, J.T., 1994. Cosmic ray contributions to dose rates for luminescence and ESR dating: large depths and long term time variations. Radiat. Meas. 23, 497–500.

Roosta, H., Jalalifar, H., Nasab, S.K., Ranjbar, M., 2019. Seven years of surface deformation above the buried Nasr-Abad salt diapir using InSAR time-series analysis, Central Iran. Journal of Geodynamics 130, 1–11.

Rostami, H., Richter, T., Ruter, A.H., Azizi, G., Darabi, H., 2024. High-resolution, multi-proxy reconstruction of central Zagros paleoclimate and paleoenvironment from the Late Pleistocene to the Holocene. Quat. Int. 692, 45–55.

Ruh, J.B., Hirt, A.M., Burg, J.P., Mohammadi, A., 2014. Forward propagation of the Zagros Simply Folded Belt constrained from magnetostratigraphy of growth strata. Tectonics 33, 1534–1551.

Sepehr, M., Cosgrove, J.W., 2004. Structural framework of the Zagros fold–thrust belt, Iran. Marine and Petroleum Geology 21, 829–843.

Shami, S., Shahriari, M.A., Nilfouroushan, F., Forghani, N., Salimi, M., Reshadi, M.A.M., 2024. Surface displacement measurement and modeling of the Shah-Gheyb salt dome in southern Iran using InSAR and machine learning techniques. Int. J. Appl. Earth Obs. Geoinf. 132, 104016.

Sherkati, S., Letouzey, J., Frizon de Lamotte, D., 2006. Central Zagros fold-thrust belt (Iran): New insights from seismic data, field observation, and sandbox modeling. Tectonics 25, TC4007.

Snidero, M., Muñoz, J.A., Carrera, N., Butillé, M., Mencos, J., Motamedi, H., Piryaei, A., Sàbat, F., 2019. Temporal evolution of the Darmadan salt diapir, eastern Fars region, Iran. Tectonophysics 766, 115–130.

Stöklin, J., 1968. Structural history and tectonics of Iran: a review. Am. Assoc. Pet. Geol. Bull. 52, 1229–1258.

Talbot, C.J., 1979. Fold trains in a glacier of salr in southern Iran. Journal of Structural Geology 1, 5–18.

Talbot, C., Aftabi, P., 2004. Geology and models of salt extrusion at Qum Kuh, central Iran. J. Geol. Soc. London 161, 321–334.

Talbot, C.J., Alavi, M., 1996. The past of a future syntaxis across the Zagros. Geological Society, London, Special Publication 100, 89–109.

Talbot, C.J., Jarvis, R.J., 1984. Age, budget and dynamics of an active salt extrusion in Iran. Journal of Structural Geology 6, 521–533.

Talbot, C.J., Pohjola, V., 2009. Subaerial salt extrusions in Iran as analogues of ice sheets, streams and glaciers. Earth Sci. Rev. 97, 155–183.

Talbot, C.J., Medvedev, S., Alavi, M., Shahrivar, H., Heidari, E., 2000. Salt extrusion at Kuh-e-Jahani, Iran, from June 1994 to November 1997. In: Vendeville, B., Mart, Y., Vigneresse, J.L. (Eds.), Salt, Shale and Igneous Diapirs in and around Europe, Geological Society, London, Special Publication, 174, pp. 93–110.

Talebian, M., Jackson, J., 2004. A reappraisal of earthquake focal mechanisms and active shortening in the Zagros mountains of Iran. Geophys. J. Int. 156, 506–526.

Tavakoli, F., Walpersdorf, A., Authemayou, C., Nankali, H.R., Hatzfeld, D., Tatar, M., Djamour, Y., Nilforoushan, F., Cotte, N., 2008. Distribution of the right-lateral strike–slip motion from the Main Recent Fault to the Kazerun Fault System (Zagros, Iran): evidence from present-day GPS velocities. Earth Planet. Sci. Lett. 275, 342–347.

Tayebi, M.H., Tangestani, M.H., Roosta, H., 2013. Mapping salt diapirs and salt diapir-affected areas using MLP neural network model and ASTER data. International Journal of Digital Earth 6 (2), 143–157.

Vergés, J., Emami, H., Garcés, M., Beamud, E., Homke, S., Skott, P., 2019. Zagros foreland fold belt timing across Lurestan to constrain Arabia-Iran collision. In: Saein, A.F. (Ed.), Developments in Structural Geology and Tectonics, 3. Elsevier, Amsterdam, pp. 29–52.

Vernant, P., Nilforoushan, F., Hatzfeld, D., Abbassi, M.R., Vigny, C., Masson, F., Nankali, H., Martinod, J., Ashtiani, A., Bayer, R., Tavakoli, F., Chéry, J., 2004. Present-day crustal deformation and plate kinematics in the Middle East constrained by GPS measurements in Iran and northern Oman. Geophys. J. Int. 157, 381–398.

Walpersdorf, A., Hatzfeld, D., Nankali, H., Tavakoli, F., Nilforoushan, F., Tatar, M., Vernant, P., Chéry, J., Masson, F., 2006. Difference in the GPS deformation pattern of North and Central Zagros (Iran). Geophys. J. Int. 167, 1077–1088.

Wells, D.L., Coppersmith, K.J., 1994. New empirical relationships among magnitude, rupture length, rupture width, rupture area, and surface displacement. Bull. Seismol. Soc. Am. 84, 974–1002.

Wessel, B., 2016. TanDEM-X Ground Segment – DEM Products Specification Document. EOC, DLR, Oberpfaffenhofen, Germany, Public Document TD-GS-PS-0021. Issue 3.2, 2016. [Online]. Available: https://tandemx-science.dlr.de/.

Wright, T.J., Parsons, B.E., Lu, Z., 2004. Toward mapping surface deformation in three dimensions using InSAR. Geophys. Res. Lett. 31 (1), L01607.

Yunjun, Z., Fattahi, H., Amelung, F., 2019. Small baseline InSAR time series analysis: Unwrapping error correction and noise reduction. Comput. Geosci. 133, 104331.

Zarei, M., Raeisi, E., Talbot, C., 2012. Karst development on a mobile substrate: Konarsiah salt extrusion, Iran. Geological Magazine 149, 412–422.